ORIGINAL ARTICLE

From microanalysis to supercontinents: Insights from the Rio Apa Terrane into the Mesoproterozoic SW Amazonian Craton evolution during Rodinia assembly

Bruno V. Ribeiro[1] | Melanie A. Finch[1,2] | Peter A. Cawood[1] |
Frederico M. Faleiros[3] | Timothy D. Murphy[4] | Alexander Simpson[5] |
Stijn Glorie[5] | Mahyra Tedeschi[6] | Robin Armit[1] | Vitor R. Barrote[1,7]

[1]School of Earth, Atmosphere and Environment, Monash University, Clayton, Victoria, Australia

[2]Department of Earth and Environmental Sciences, James Cook University, Townsville, Queensland, Australia

[3]Department of Mineralogy and Geotectonics, University of São Paulo, São Paulo, Brazil

[4]ARC Centre of Excellence for Core to Crust Fluid Systems and GEMOC, Department of Earth and Planetary Sciences, Macquarie University, North Ryde, New South Wales, Australia

[5]Department of Earth Science, School of Physical Sciences, The University of Adelaide, Adelaide, South Australia, Australia

[6]CPMTC-IGC, Federal University of Minas Gerais, Belo Horizonte, Brazil

[7]Institut für Geologische Wissenschaften, Geochemie, Freie Universität Berlin, Berlin, Germany

Correspondence
Bruno Vieira Ribeiro, School of Earth, Atmosphere and Environment, Monash University, 9 Rainforest Walk, Clayton, VIC 3800, Australia.
Email: bruno.vieiraribeiro1@monash.edu

Abstract

Deciphering the tectono-metamorphic evolution of Precambrian terranes can be difficult due to reworking by later superimposed events. Whole-rock elemental and isotopic geochemistry and zircon U–Pb geochronology are often employed in those studies, but these approaches are often not sensitive to the presence of multiple events and medium-grade metamorphic episodes. The Rio Apa Terrane (RAT), an allochthonous fragment of the Amazonian Craton, is a crustal block with a well-characterized crustal evolution but with no detailed thermal constraints for its tectono-metamorphic evolution. In contrast to previous studies, we show the existence of four tectono-metamorphic events at $c.$ 1,780, $c.$ 1,625, $c.$ 1,420–1,340, and $c.$ 1,300–1,200 Ma on the basis of apatite, titanite, and rutile U–Pb, in situ white-mica Rb–Sr, and in situ garnet Lu–Hf geochronology combined with mineral chemistry and phase-equilibria modelling. The $c.$ 1,780 Ma event is recorded in the basement of the Western domain, representing an extensional event coeval with the development of its Eastern domain in response to the retreat stage of the accretionary system. This is followed by juxtaposition of the Western and Eastern domains along a major crustal boundary at $c.$ 1,625 Ma, which is defined by the magnetic profiles and zircon U–Pb–Hf data across the boundary. The third and fourth events correspond to progressive high-pressure/medium-temperature (HP/MT) metamorphism, characterized by an anticlockwise P–T path, suggesting a convergent-to-collisional tectonic setting. The RAT was accreted to the adjoining Paraguá Terrane at $c.$ 1,420–1,340 Ma under an isobaric P–T evolution spanning ∼530°C to 600°C and ∼10.0 kbar. Subsequently, the combined Rio Apa and Paraguá terranes collided with the SW Amazonian Craton at $c.$ 1,300–1,200 Ma, reaching P–T conditions of ∼560–580°C and ∼10.9–11.7 kbar during crustal thickening. This study reveals for the first time the existence of a HP/MT metamorphic evolution related to the growth of the SW Amazonian Craton as part of an accretionary orogenic system during Rodinia assembly in the Palaeoproterozoic to Mesoproterozoic.

1 | INTRODUCTION

The tectonic evolution of complex Precambrian terranes can be challenging to disentangle, requiring a multi-method approach to reveal the magmatic and metamorphic-deformational events. The magmatic history is generally revealed with whole-rock and in situ geochemistry and isotopic analyses (e.g., Alves et al., 2013; Cioffi et al., 2016). However, the metamorphic-deformational events can be followed by modifier processes that obscure the record of these events (metamorphic overprints, metasomatism, etc.), making the post-magmatic evolution generally more difficult to unravel (Lanari et al., 2013; Lanari & Duesterhoeft, 2019). Typically, these modifying processes do not affect all minerals and/or isotopic systems in the same way, so employing a diverse range of analytical techniques on a variety of mineral phases can reveal the entire tectono-metamorphic history (Cioffi et al., 2019; Holder et al., 2019; Kirkland et al., 2017, 2020; Pollington & Baxter, 2010; Rocha et al., 2017). Geochronological and geochemical studies of ancient terranes commonly contribute to supercontinent reconstructions; however, better tectonic inferences may be made when the timing and conditions of metamorphism are also considered (e.g., Volante et al., 2020; Wan et al., 2015).

The Palaeoproterozoic to Mesoproterozoic Rio Apa Terrane (RAT), an allochthonous fragment of the Amazonian Craton (Figure 1a), is an example of a long-lived accretionary orogen developed along the SW Amazonian margin (Cordani et al., 2010; Faleiros et al., 2016; Ribeiro, Cawood, et al., 2020; Teixeira et al., 2020), which has undergone a long and complex metamorphic evolution. The RAT is predominantly composed of (meta)igneous and subordinate metasedimentary rock units ranging from 2,100 to 1,720 Ma, overprinted by regional thrusting at c. 1,300 Ma (Figure 1b,c) (Cordani et al., 2010; Ribeiro, Cawood, et al., 2020; Teixeira et al., 2020). Although the crustal development of the RAT is well studied on the basis of whole-rock geochemistry and zircon dating and isotopic studies (U–Pb–Hf) (Faleiros et al., 2016; Lacerda Filho et al., 2016, 2020; Plens, 2018; Plens et al., 2013; Ribeiro, Cawood, et al., 2020; Teixeira et al., 2020, and references therein), the tectono-metamorphic events are poorly constrained, leading to uncertain tectonic inferences.

Two tectono-metamorphic events were proposed for the RAT at c. 1,670 and c. 1,300 Ma (Cordani et al., 2010). Although the 1,300 Ma event is well recorded in multi-mineral K/Ar, $^{40}Ar/^{39}Ar$, and monazite U–Pb ages (Cordani et al., 2010; Lacerda Filho et al., 2016, 2020), the '1,670 Ma event' was solely inferred from whole-rock Rb–Sr isochron age data and has never been reported by any robust in situ mineral dating. The latter event is suggested to reflect regional medium- to high-grade metamorphism in response to the closure and consolidation of the RAT as a coherent terrane, supporting further relations with Nuna and Rodinia supercontinents (Cordani et al., 2010; Lacerda Filho et al., 2020; Teixeira et al., 2020). Considering the importance of this age for tectonic reconstructions of the RAT and the overall SW Amazonian region during the Mesoproterozoic, a detailed investigation using advanced petrochronology is required.

In this contribution, we present the first petrochronological investigation of the RAT using phase-equilibria modelling coupled to state-of-the-art geochronology (U–Pb–REE in apatite, titanite, rutile, in situ Lu–Hf in garnet, and in situ Rb–Sr in white-mica) to elucidate the tectono-metamorphic events that affected the terrane. We also integrate field-based structural analysis with airborne magnetic data and zircon U–Pb–Hf signatures to investigate the existence of a Mesoproterozoic large-scale suture zone. Our findings demonstrate the power of using a multi-disciplinary approach applied to key rock samples, providing new insights, and challenging the Mesoproterozoic tectono-metamorphic evolution of the SW Amazonia margin.

2 | GEOLOGICAL SETTING

The RAT is a fragment of the Amazonia Craton and is predominantly composed of (meta)igneous and metasedimentary rocks, covered by the Neoproterozoic-Cambrian Corumbá Group and the Quaternary Pantanal Formation (Figure 1b) (Affonso et al., 2021; Faleiros et al., 2016; Ribeiro, Cawood, et al., 2020; Rocha et al., 2019; Teixeira et al., 2020). Based on whole-rock Sm–Nd and zircon U–Pb isotopic data, the RAT was divided into Western and Eastern Terranes bounded by the Aldeia Tomázia Shear Zone, a mostly concealed N-S-trending structure interpreted to represent a major suture
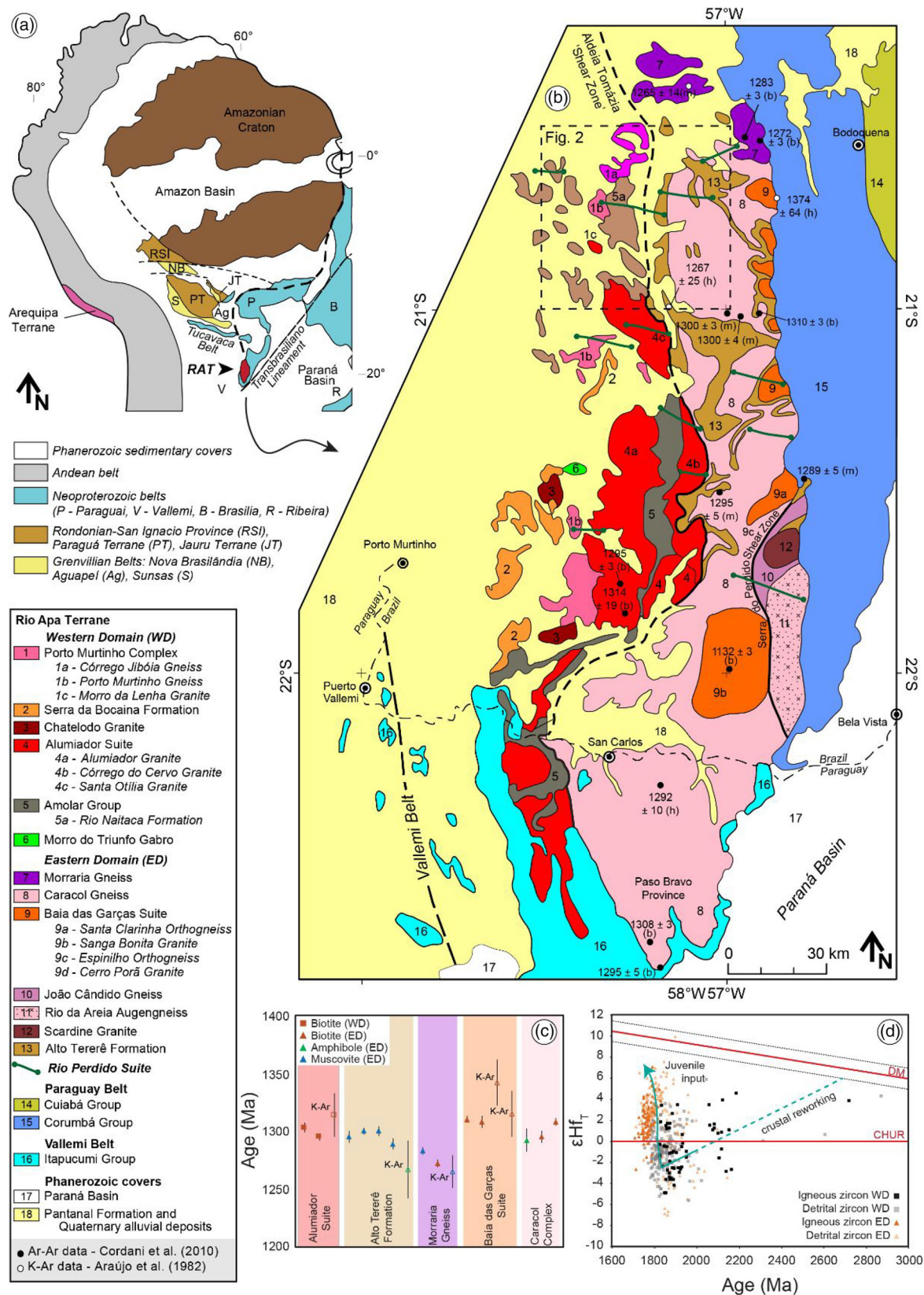
FIGURE 1 (a) Regional context of the RAT in relation to the SW Amazonia Craton and adjoining terranes and orogenic belts (adapted from Faleiros et al., 2016); (b) geological map of the RAT indicating K–Ar and $^{40}Ar/^{39}Ar$ ages from the main units (adapted from Ribeiro, Cawood, et al., 2020); (c) summary of multi-mineral K–Ar and $^{40}Ar/^{39}Ar$ (data extracted from Cordani et al., 2010); (d) εHf_T versus zircon crystallization age from the Western and Eastern domains of the RAT (zircon data extracted from Ribeiro, Cawood, et al., 2020) [Colour figure can be viewed at wileyonlinelibrary.com]

(Cordani et al., 2010; Faleiros et al., 2016). Zircon U–Pb–Hf data collected across the RAT suggest that the Western and Eastern Terranes were developed during advancing and retreating episodes of a single accretionary orogenic system, following a crustal reworking trend (from *c.* 2.7 to 1.8 Ga) and input of more juvenile magmatism (*c.* 1.8 to 1.72 Ga) due to a possible slab roll back (Figure 1d; Ribeiro, Cawood, et al., 2020). Given that both 'terranes' share a genetic relationship, we will adopt the terms Western and Eastern domains hereafter to avoid the tectonic significance of the term 'terrane'.

Although the magmatic evolution of the RAT is well investigated (e.g., Brittes et al., 2013; Dos Santos et al., 2019; Lacerda Filho et al., 2016; Manzano et al., 2012; Plens, 2018; Plens et al., 2013; Souza et al., 2017), the tectono-metamorphic evolution is uncertain. It is proposed that the RAT consolidated as a single coherent and stable tectonic unit at *c.* 1.67 Ga on the basis of whole-rock Rb–Sr ages, interpreted to record a medium- to high-grade metamorphic event inferred to be related to amalgamation of the RAT (Cordani et al., 2010). This interpretation has been adopted in the subsequent literature and has been used to support tectonic reconstructions of the RAT within Nuna and Rodinia (Lacerda Filho et al., 2016, 2020; Redes et al., 2020; Teixeira et al., 2020). K–Ar and ^{40}Ar/^{39}Ar dating across the RAT demonstrated the existence of a regional thermal event at *c.* 1,300 Ma (Araújo et al., 1982; Cordani et al., 2010; Lacerda Filho et al., 2020), which is also identified in metamorphic monazite (Lacerda Filho et al., 2016). Since the *c.* 1,300 Ma event is also present in the SW Amazonian Craton, it was inferred that the RAT was at its periphery at that time (Teixeira et al., 2020). The metasedimentary rock sequence of the Eastern domain (Alto Tererê Formation; Figure 1b) is inferred to record a Barrovian-type metamorphic sequence from field-based observations of a progression from the biotite to the garnet zones and localized staurolite and kyanite zones (Faleiros et al., 2016). As it is the only reported metasedimentary rocks in the RAT with key metamorphic mineral assemblages, it is the rock sequence most likely to record the full tectono-metamorphic evolution.

2.1 | Study area

This paper focuses on the Porto Murtinho Complex, Caracol Complex, and the Alto Tererê Formation exposed in the northern region of the RAT (Figure 2a). The Porto Murtinho Complex is composed of mylonitic monzonitic orthogneiss (Córrego Jiboia Gneiss) and undeformed porphyritic monzogranite (Morro da Lenha Granite) generally with high-K calc-alkaline geochemical

signature (Faleiros et al., 2014, 2016). The Caracol Complex, the characteristic unit of the Eastern domain, is composed of polydeformed leucocratic gneiss of granitic composition typically with high-K calc-alkaline geochemical signatures and dominantly suprachondritic zircon εHf$_T$ (Plens, 2018; Ribeiro, Cawood, et al., 2020; Teixeira et al., 2020). The Alto Tererê Formation represents the supracrustal sequence of the Eastern domain, being composed of medium-grade siliciclastic metasedimentary rocks including schist with variable mineralogy (ranging from biotite to staurolite zone) and quartzite (from muscovite to garnet zone) with interlayered lenses of amphibolite with a precursor back-arc geochemical affinity (Faleiros et al., 2016; Lacerda Filho et al., 2016; Teixeira et al., 2020).

The Caracol Complex, previously dated with zircon U–Pb (LA-ICP-MS) at 1,756 ± 12 Ma (FMR140) and 1,786 ± 44 Ma (FMR162) (Ribeiro, Cawood, et al., 2020), strikes NNW with a shallow NE dip and shallowly ENE plunging stretching lineation. The metasedimentary rocks of the Alto Tererê Formation have a detrital zircon record indicative of derivation from the Caracol Complex (Ribeiro, Cawood, et al., 2020) and show similar structures to the Caracol Complex with a NNW-striking mylonitic foliation dipping shallowly ENE with a down-dip stretching lineation. Generally, the foliation in the RAT is N-trending with a shallow E dip, but in the north the Porto Murtinho Complex it is NW-striking and vertical with a downdip stretching lineation. The rocks here are granitic mylonites dated at 1,947 ± 9 Ma (FMR101, SHRIMP zircon U–Pb; Faleiros et al., 2016).

We selected three samples of the Porto Murtinho Complex with a NW-trending strike foliation (FMR101, FMR104, and FMR105) and one sample with a N-trending strike foliation (FMR109) in order to evaluate the age of these mylonitic foliations and their relation to the tectono-metamorphic evolution of the RAT (Figure 2). Additionally, we selected four samples of the Caracol Complex (FMR162, FMR140, FMR147, and FMR42) and two samples of the Alto Tererê Formation (FMR99 and FMR93; Figure 2) to reconstruct the pressure–temperature–time–deformation (*P–T–t–d*) evolution of the RAT.

3 | METHODS

3.1 | Geophysical analyses

High-resolution airborne magnetic data collected by the Geological Survey of Brazil between 2008 and 2009 were analysed using Oasis Montaj™ (data available from http://geosgb.cprm.gov.br). The regional magnetic signal
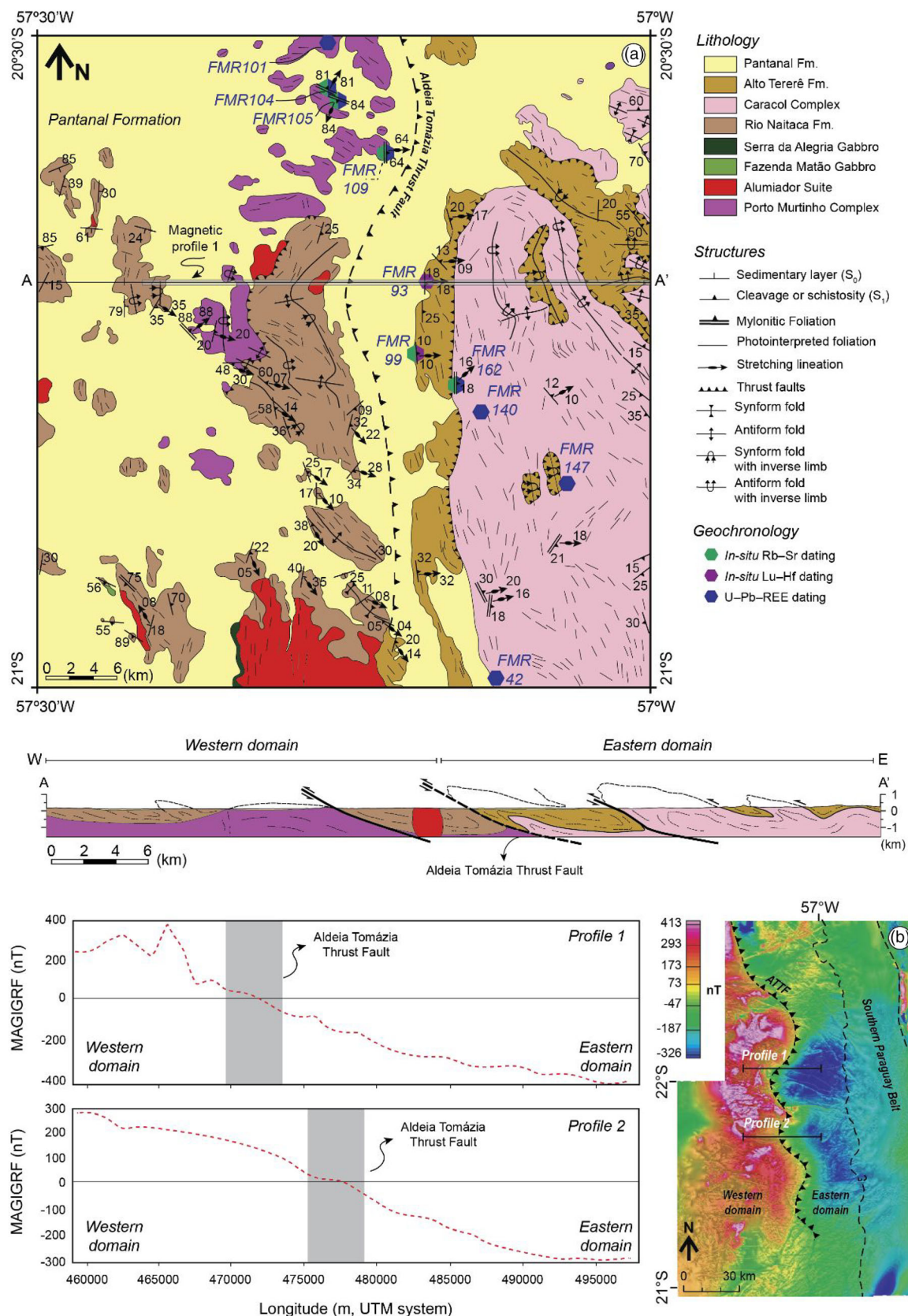
FIGURE 2 (a) Detailed map of the study area with structural features and location of samples used for geochronology and phase-equilibrium modelling (adapted from Faleiros et al., 2014). A schematic cross-section A-A′ is presented with the structural interpretation of the northern sector of the RAT; (b) composite map with reduced-to-pole (RTP) magnetic map overlayed by the tilt derivative in greyscale (right) and magnetic profiles sampled across the study area (left) [Colour figure can be viewed at wileyonlinelibrary.com]

was corrected using the international geomagnetic reference field (IGRF) and reduced to the pole (RTP) filter to remove the effect of the earth's magnetic inclination and declination in this part of Brazil. A tilt derivative of the RTP data is overlaid in grey to better identify high-frequency features and the edges of magnetic anomalies (Figure 2b). Magnetic profiles were constructed by sampling the corrected magnetic signal along two profiles across the RAT.

3.2 | Electron probe microanalyser

Chemical mineral compositions were acquired using a CAMECA SX100s at the Macquarie Analytical and Workshop Facility, Macquarie University, Australia. The experiments were performed using an acceleration voltage of 15 keV, probe current of 20 nA, and spot-size of 1 μm. For the calibration procedures, the following standards were employed: Si, Mg, Al (biotite), Na (albite), K (orthoclase), Ca ($CaSiO_3$), Ti (rutile, TiO_2), Cr (chromite), Mn (Mn-garnet), Fe (magnetite, Fe_2O_3), P (apatite), and F (AlF_3). Total iron was taken as FeO.

X-ray maps (Si, Al, Fe, Ca, Mn, Mg, K, Na) were acquired in two passes (e.g., Lanari et al., 2019) using a CAMECA SX100s. The analyses were performed using an accelerating voltage of 15 keV, probe current of 90 nA, step-size of 3 to 5 μm, and dwell time of 150 ms. Garnet compositional maps were calibrated against point analyses using XMapTools 3.4.1 (Lanari et al., 2014, 2019) assigning the specific composition of each pixel across the garnet zones. The average composition of each zone in oxide content (wt%), oxygen-normalized element per formula unit (p.f.u.), and garnet end-members were determined by integrating the pixel composition of each garnet zone (e.g., Santamaría-López et al., 2019). Compositional domains from each zone were carefully selected avoiding mixing pixels, mineral inclusions, and boundaries potentially affected by diffusion. Mineral compositions and associated uncertainties are presented in Supporting Information S1.

3.3 | Phase-equilibria modelling

Phase-equilibria modelling considered the whole-rock bulk composition and was performed using Perple_X'6.9.1 with 10 components (SiO_2–TiO_2–Al_2O_3–FeO–MgO–CaO–Na_2O–K_2O–O_2–H_2O) using the database of end-member mineral thermodynamic properties of Holland and Powell (2011) (version hp633ver adapted for Perple_X) and the following activity–composition relationships: Gt(W), Bi(W), Mica(W), Chl(W), and Crd(W)

from White et al. (2014), ilmenite from White et al. (2014, 2000), and feldspar from Fuhrman and Lindsley (1988). The water content was estimated so that the rock was saturated at first melt. The intersections of almandine (Alm), spessartine (Spss), and grossular (Grs) isopleths constrain the P–T conditions of garnet crystallization with relative errors associated to the uncertainties of the electron probe microanalyser (EPMA) data (cf. Lanari et al., 2017) assuming the premise of x(Alm) + x(Sps) + x(Grs) $\sim$ 1 with very low pyrope contents. These isopleths were cross-checked with isopleths of Si (p.f.u.) in white-mica. Mineral abbreviations follow Whitney and Evans (2010).

3.4 | Geochronology

3.4.1 | In situ U–Pb–REE analyses

Multi-mineral U–Pb–REE analyses were performed via laser ablation split stream inductively coupled plasma mass spectrometry (LASS-ICP-MS) at the Isotopia Laboratory, School of Earth, Atmosphere and Environment, Monash University, Australia. The experiments were performed using an ASI RESOLution 193 nm ArF excimer laser ablation system equipped with a dual volume Laurin Technic S155 ablation cell. U and Pb isotopes were measured using a Thermo Scientific iCAP triple quadrupole TQ-ICP-MS, and trace element concentrations were measured using an iCAP Q-ICP-MS. The analytical routines for apatite, titanite, and rutile are detailed described elsewhere (see Ribeiro, Mulder, et al., 2020; Zoleikhaei et al., 2021). Data reduction was performed in Iolite4 using the built-in data reduction schemes for U–Pb (no common-Pb correction considered) and trace elements (Paton et al., 2010, 2011). U–Pb ages were calculated using IsoplotR (Vermeesch, 2018) with no common-Pb correction considered. All ages and uncertainties are presented with 2σ level of confidence with final ages presented as $x \pm |y|$, with x representing the age (Ma) and $|y|$ representing the studentized error stated at 95% confidence (Vermeesch, 2018). We used [43]Ca as an internal standard for apatite, [14]Si for titanite, and [49]Ti for rutile assuming the average stochiometric proportion. MADEL (Payne et al., 2008), BLR (Aleinikoff et al., 2007), and Sugluk-4 (Bracciali et al., 2013) were employed as primary standard for apatite, titanite, and rutile U–Pb analyses, respectively. The following standards were employed as unknown for the purpose of accuracy checks during U–Pb analyses: monazite 44069 (Aleinikoff et al., 2006), and Madagascar apatite (Thomson et al., 2012), OLT titanite (Kennedy et al., 2010), and R632 rutile (Axelsson et al., 2018). The

44069 monazite yielded an average ^{206}Pb/^{238}U age of 422 ± 2 Ma (MSWD = 0.3, N = 100), Madagascar apatite yielded an ^{207}Pb-corrected age (using the in-built Stacey and Kramers, 1975, correction in IsoplotR) of 490 ± 6 Ma (MSWD = 0.6, N = 32), OLT titanite yielded a concordia age of 1,009 ± 7 Ma (MSWD = 2.7, N = 13), and R632 rutile yielded a concordia age of 497 ± 5 Ma (MSWD = 1.1, N = 7). All secondary standards yielded ages in agreement with reference values for each standard and to the long-term reproducibility of the Isotopia Lab results (e.g., Ribeiro, Lagoeiro, et al., 2020; Ribeiro, Mulder, et al., 2020; Zoleikhaei et al., 2021).

The international glass NIST610 was employed as primary standard for trace element analyses. All U–Pb and trace element secondary standards match with the reference values and the laboratory long-term reproducibility. Secondary standards for trace element analyses (NIST612, BCR2, ATHO) yield an accuracy of 1%–5% in comparison with the reference values. The complete data set of all samples is presented in Supporting Information S2 (apatite), S3 (titanite), and S4 (rutile). U–Pb and REE standard results are presented in Supporting Information S5.

3.4.2 | In situ Rb–Sr analyses

White-mica Rb–Sr analyses were performed at the Isotopia Laboratory, School of Earth, Atmosphere and Environment, Monash University, Australia. The experiments were performed using an ASI RESOLution 193 nm ArF excimer laser ablation system equipped with a dual volume Laurin Technic S155 ablation cell coupled to a Thermo Scientific iCAP TQ-ICP-MS. The ablation was performed in a He atmosphere with the following laser setting: energy density of 3 J/cm^2, 10 Hz frequency, and 100 μm spot-size. Each analysis consists of 20 s background acquisition followed by 30 s ablation time. Isobaric interferences between ^{87}Rb and ^{87}Sr were removed by introducing N$_2$O$_{(g)}$ (0.15 ml/min) into the TQ-collision cell (Hogmalm et al., 2017; Zack & Hogmalm, 2016). NIST 610 was employed as the primary standard for calibrating the ^{87}Sr/^{86}Sr ratios, whereas the pressed powder tables of phlogopite Mica-Mg were employed as a primary standard to calibrate the ^{87}Rb/^{86}Sr ratios. Biotite from the Round Flat tonalite (zircon U–Pb age of 415.5 ± 7.2 Ma) (Kemp et al., 2005) was employed as the secondary standard, yielding a feldspar-anchored Rb–Sr isochron age of 409.6 ± 6.2 Ma (n = 20, MSWD = 0.16). Data reduction was performed using Iolite 4 (Paton et al., 2010, 2011) using an in-house data reduction scheme. Rb–Sr isochrons and ages were calculated using IsoplotR (Vermeesch, 2018) with the Rb decay constant

after Villa et al. (2015). All ages and uncertainties are presented with 2σ level of confidence with final ages presented as $x \pm |y|$, with x representing the age (Ma) and $|y|$ representing the studentized error stated at 95% confidence (Vermeesch, 2018). The complete data set of all samples is presented in Supporting Information S6.

3.4.3 | In situ Lu–Hf analyses

In situ Lu–Hf analyses were conducted at Adelaide Microscopy, University of Adelaide, following the methodology outlined in Simpson et al. (2021). Garnet grains were mounted in epoxy mounts and analysed using a RESOLution 193 excimer laser system coupled to an Agilent 8900 ICP MS/MS, using a 'squid' mixing device (Laurin Technic) smoothing the laser pulses. The experiments were focused in the centre of each garnet grain aiming to date the core using a laser setting of 3.0 J/cm^2 energy fluency, 10 Hz repetition rate, and 67 μm spot-size. Data acquisition was performed with 30 s of background collection followed by 40 s acquisition time (ablation). Additional N$_2$ (3.5 ml/min) was added to the carrier gas to enhance sensitivity (Hu et al., 2008). Reaction gas composed of 10% NH$_3$ and 90% He was introduced into the collision cell at a flow rate of 3 ml/min to remove isobaric interferences on ^{176}Hf (Simpson et al., 2021).

The international glass NIST610 was used as the primary reference material in order to correct for analytical drift and reactivity differences between Lu and Hf. A ^{176}Lu/^{177}Hf ratio of 0.1379 ± 0.005 and ^{176}Hf/^{177}Hf ratio of 0.282111 ± 0.000009 were used to calibrate analyses (Nebel et al., 2009). The Hogsbo garnet was used to correct for the effects of matrix-induced elemental fractionation, producing an age of 1,063 ± 8 Ma compared with the expected age of 1,029 ± 1.7 Ma (Romer & Smeds, 1996). An in-house secondary standard was used as quality control (Black Point 1), yielding a corrected age of 1,759 ± 12 Ma (MSWD = 1.2), similar to the expected age of c. 1,745 Ma (Lane, 2011).

Background subtractions, drift correction, and primary standard normalization were processed using LADR software (Norris & Danyushevsky, 2018). Isochron ages were calculated using IsoplotR (Vermeesch, 2018) with a ^{176}Lu decay constant after Söderlund et al. (2004). All ages and uncertainties are presented with 2σ level of confidence with final ages presented as $x \pm |y|$, with x representing the age (Ma) and $|y|$ representing the studentized error stated at 95% confidence (Vermeesch, 2018). In situ Lu–Hf data were treated in inverse isochron diagrams to minimize error correlations between isochron ratios (Li & Vermeesch, 2021). The

complete data set for unknown and standards is presented in Supporting Information S7.

4 | RESULTS

4.1 | Rocks and microstructures

The meta-igneous rocks from both Western and Eastern domains of the RAT are strikingly similar, being primarily composed of quartz, alkali-feldspar, plagioclase, white-mica, and occasionally garnet (Figure 3a–f). Late-stage sericite and epidote are common in most rocks of the RAT. Rock samples from the Porto Murtinho Complex (Western domain) and the Caracol Complex (Eastern domain) have protomylonitic to mylonitic foliations mostly defined by preferred orientation of white-mica, elongated quartz-rich, and sericite-rich aggregates. Despite the similar mineral assemblages, the rocks from both complexes preserve distinct quartz microstructures.

Quartz aggregates from rocks of the Porto Murtinho Complex display external sigmoidal shapes with inter-lobate to serrate grain boundaries surrounded by neoformed grains up to tens of μm in size (Figure 3a–d). Large grains with clear patchy undulose and subgrains are common (Figure 3c). This set of quartz microstructures indicates that quartz initially recrystallized through grain boundary migration later overprinted by bulging recrystallization (BLG), qualitatively indicating a temperature gradient from ~500°C to ~300°C (Faleiros et al., 2010; Stipp et al., 2002a, 2002b). On the other hand, quartz grains from rocks of the Caracol Complex are embedded in a protomylonitic structure with coarse
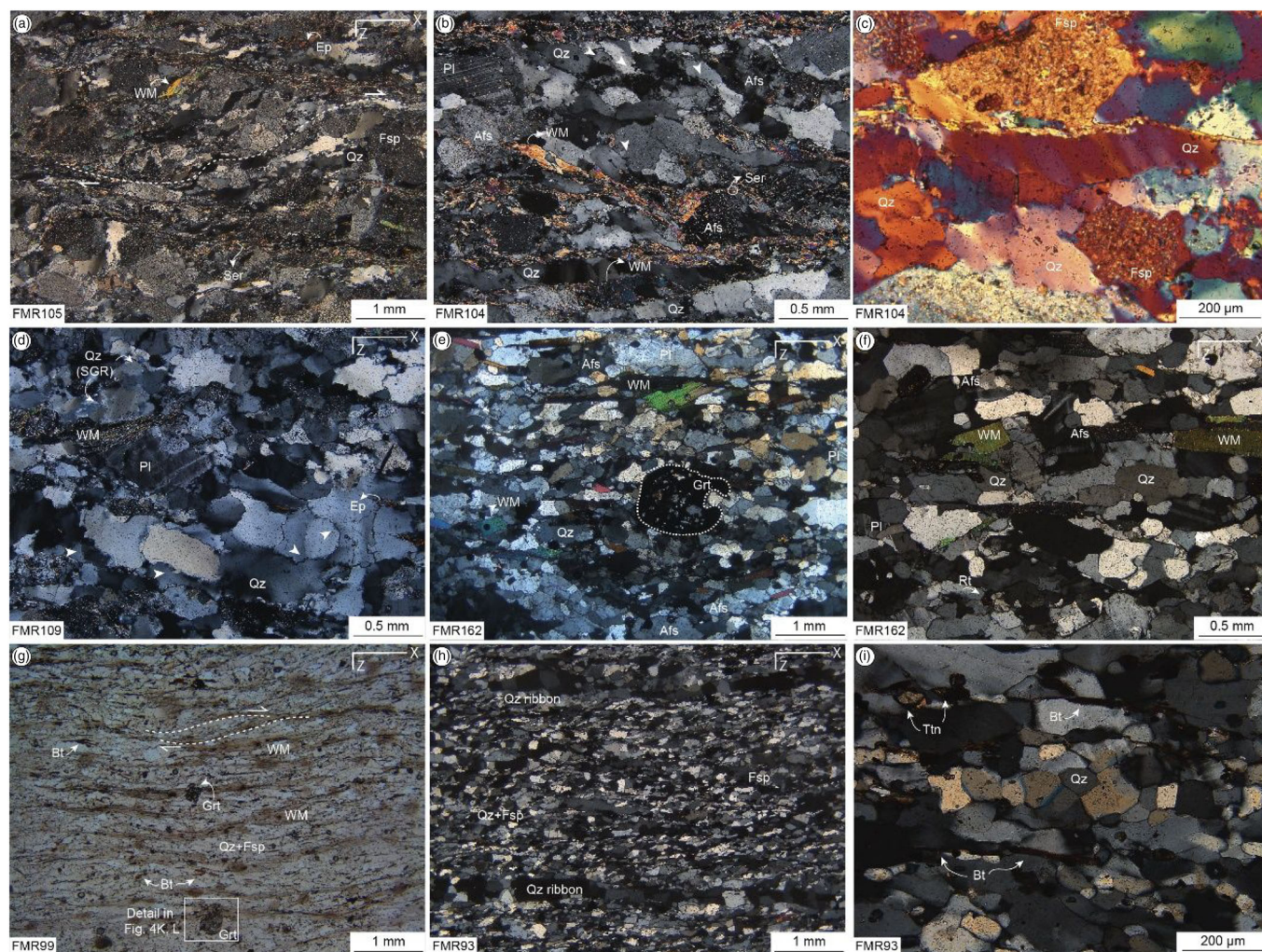
FIGURE 3 Photomicrographs of rock samples from the Rio Apa Terrane. (a–d) Granitic mylonite samples of the Porto Murtinho Complex; (e) granitic mylonite of the Caracol Complex; (g–i) metasedimentary rocks of the Alto Tererê Formation. White arrows in photomicrographs (b) and (d) indicate quartz bulging. All photomicrographs were taken under cross-polarized light, except photomicrograph (g) that was taken under plane-polarized light [Colour figure can be viewed at wileyonlinelibrary.com]

plagioclase and feldspar with a shape preferred orientation parallel to the X-direction defining the rock structure (Figure 3e). Quartz is mostly euhedral to subhedral, inequigranular with interlobate to polygonal grain boundaries with weak or no undulose extinction, commonly pinned by white-mica grains. These microstructures indicate that quartz was recrystallized by grain boundary migration (∼500°C; Faleiros et al., 2010; Stipp et al., 2002b), potentially achieving grain boundary area reduction and recovery (Passchier & Trouw, 2005).

The Alto Tererê Formation encompass mica-schist, sometimes with garnet (Figure 3g) and meta-arkose (Figure 3h). The mica-schist (sample FMR99) is primarily composed of quartz, plagioclase, alkali-feldspar, white-mica, and biotite and garnet both in low proportions (<2%). Epidote, zoisite, and clinozoisite are common throughout the rock and are generally associated with hydrothermal alteration. The structure is mostly defined by the shape preferred orientation of white-mica, developing a S/C fabric with clockwise shear sense (Figure 3g). Garnet grains are described in detail below (Section 4.2.4). The meta-arkose (sample FMR93) is primarily composed of quartz and feldspar forming a granoblastic matrix with fined-grained titanite and biotite oriented parallel to the X-direction (Figure 3h,i). Quartz grains in the matrix display oblique shape preferred orientation indicating a clockwise shear sense, whereas quartz aggregates are oriented parallel to the X-direction. Quartz grains are mostly euhedral, equigranular with straight grain boundaries (polygonal) with few or no undulose extinction (Figure 3i). These microstructures suggest that quartz was affected by static recrystallization through grain boundary area reduction and recovery under high temperature conditions (>500°C) (Passchier & Trouw, 2005).

4.2 | Accessory mineral phases

4.2.1 | Apatite

Apatite from sample FMR101 of the Porto Murtinho Complex is commonly subhedral, inclusion-free, and usually associated with biotite and sericite bounding quartz and feldspar grains. Apatite grains from samples FMR104 and FMR109 are commonly subhedral occurring embedded in the rock matrix and lacking any microstructural control (Figure 4b). Apatite from two samples of the Caracol Complex (FMR147 and FMR42) is anhedral, mostly rounded, and embedded in the quartz matrix, sometimes fractured, lacking any close textural relation with other accessory mineral phases (e.g., zoisite and clinozoisite).

4.2.2 | Titanite

Titanite from sample FMR101 of the Porto Murtinho Complex is euhedral, with different grain sizes (∼0.2–1.0 mm) and no relationship to the preferred orientation of the quartz matrix (Figure 4e). Titanite from sample FMR42 of the Caracol Complex is mostly euhedral to subhedral and oriented towards the metamorphic foliation, fractured, and in close association with biotite, epidote, and zoisite/clinozoisite (Figure 4f).

4.2.3 | Rutile

Rutile from two samples of the Caracol Complex (FMR140 and FMR162) is commonly anhedral in shape, located along quartz grains boundaries surrounded by fluid inclusion trails (Figure 4g, red arrows). Additionally, these fluid inclusions trails establish a connection between quartz grain boundaries and rutile embedded in quartz grains.

4.2.4 | Garnet

The single garnet porphyroblast present in the thin section from sample FMR93 of the Alto Tererê Formation is subhedral, light brown in colour, commonly fractured, with a diameter of ∼400 μm, and a few quartz inclusions dispersed throughout the grain (Figure 4i). A strain shadow is marked by quartz grains with a prominent shape preferred orientation towards the garnet porphyroblast, indicating its syn-kinematic growth. The backscatter electron image indicates multi-mineral inclusions such as titanite, epidote, biotite, and quartz generally related to internal fractures (Figure 4j). Fine-grained zircon inclusions (<5 μm) occur throughout the porphyroblast. Zoning was not detectable in the backscatter electron images.

Garnet porphyroblasts from sample FMR99 of the Alto Tererê Formation are mostly subhedral to euhedral with light brown–pink colours, sometimes fractured, and with a grain size ranging from ∼100 to 300 μm (Figure 4k). The foliation generally wraps around the porphyroblasts, indicating their pre- to syn-kinematic growth. The backscatter electron image highlights the existence of three zones (core, rim, and outer rim) with multiple quartz inclusions concentrated in the core and few zircon inclusions (∼1–3 μm) in all zones (Figure 4l). Given the diverse mineral assemblage and garnet abundance of sample FMR99, we selected this sample for mineral chemical analyses via EPMA and phase-equilibria modelling.
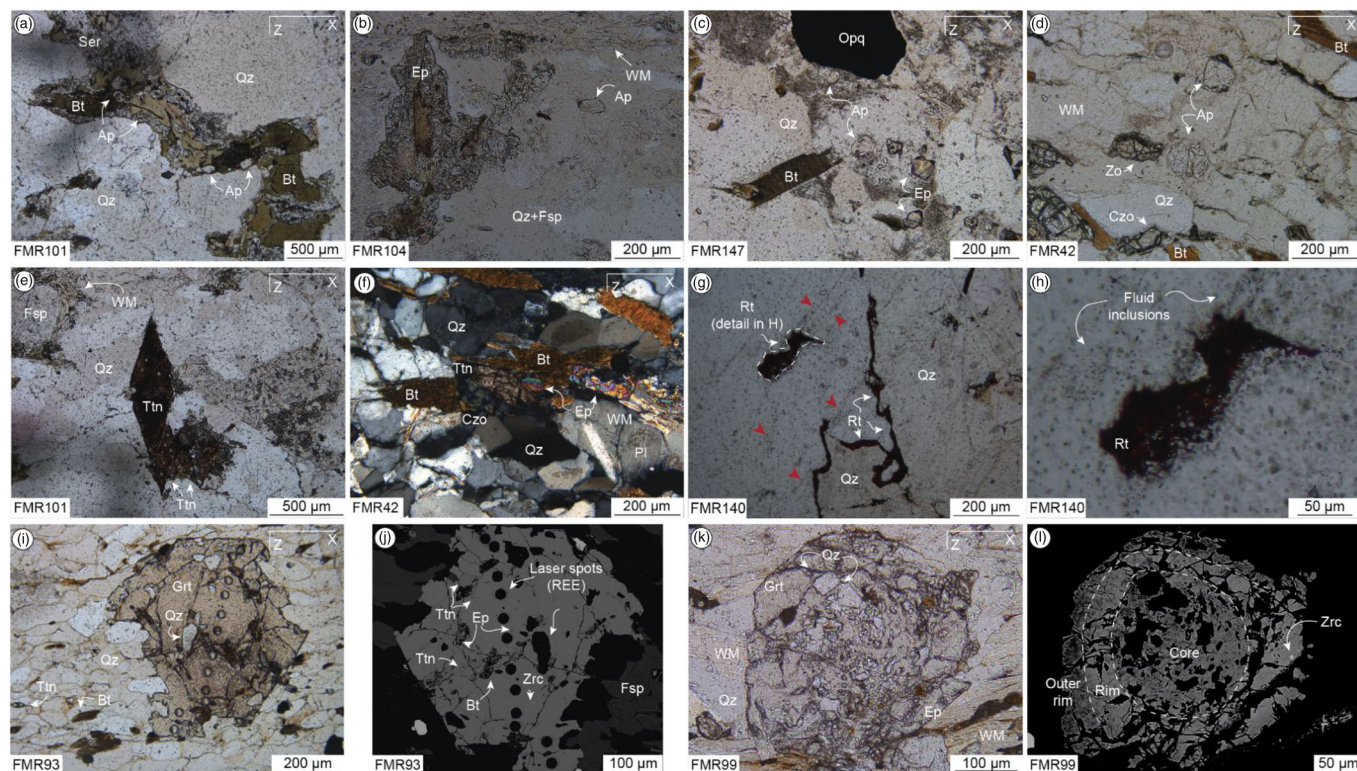
FIGURE 4 Accessory mineral phases of studied samples. Apatite from the Porto Murtinho Complex (a, b) and the Caracol Complex (c, d), titanite from the Porto Murtinho Complex (e) and Caracol Complex (f), rutile from the Caracol Complex (g, h), and garnet from the Alto Tererê Formation (i–l). Photomicrograph (f) was taken under cross-polarized light, and (a–e, g–i, k) were taken under plane-polarized light [Colour figure can be viewed at wileyonlinelibrary.com]
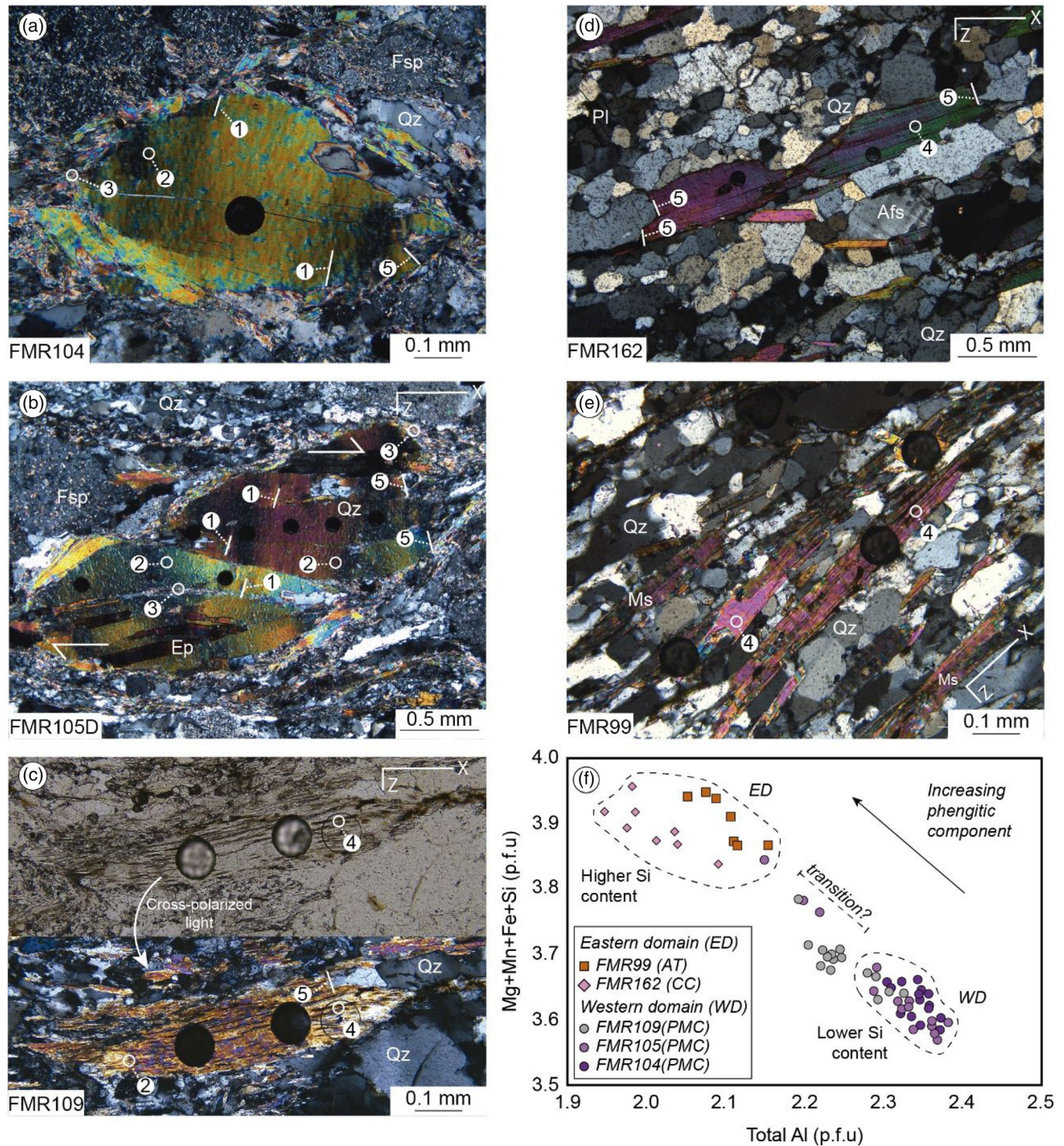
4.2.5 | White-mica

White-mica from the Porto Murtinho Complex (samples FMR104, FMR105D, and FMR109) is generally coarse-grained, displaying a fish-shaped geometry indicating clockwise shear sense for samples FMR105D and FMR109. These grains present a diverse range of microstructures such as kink bands and undulose extinction (Figure 5a–c), typically related to intracrystalline deformation and dislocation creep (Bell et al., 1986; Passchier & Trouw, 2005; Wilson & Bell, 1979). Other microstructures such as aggregates of fine-grained recrystallized white-mica forming strain shadows around fish-shaped porphyroclasts and along micro-cracks (Figure 5a,b) and grain-scale cracking at high angles to (001) planes are also common features. In addition to presenting undulose extinction and cracking at high angles to planes (001), white-mica from sample FMR109 also presents abundant exsolution of secondary phases oriented parallel to (001) planes (Figure 5c).

White-mica microstructures from the Caracol Complex (sample FMR162) and the Alto Tererê Formation (FMR99) are simpler than those from the Porto Murtinho

Complex. These grains are generally elongated and subhedral with unclear shear sense, commonly pinning quartz microstructures (Figure 5d,e). They have acicular inclusions (Fe-oxides) with a shape-preferred orientation parallel to (001) planes and grain-scale cracking at high angles to (001) planes. Moreover, microstructures related to intracrystalline deformation such as kink-bands and undulose extinction are scarce.

In addition to their distinct microstructures, white-mica from the Western and Eastern domains also show significant chemical differences. White-mica from the Porto Murtinho Complex has an average Si (p.f.u.) spanning 3.32–3.34, total Al of 2.25–2.34 (p.f.u), and average Mg+Mn+Fe+Si (p.f.u.) ranging between 3.63 and 3.69 (Figure 5f). White-mica from the Caracol Complex (FMR162) and the Alto Tererê Formation (FMR99) from the Eastern domain have a higher average Si (p.f.u.) content between 3.39 and 3.42, lower Al (p.f.u.) content of 2.09–2.10, and higher Mg+Mn+Fe+Si (p.f.u.) spanning 3.89–3.91. Considering the Tschermak substitution in white-mica, Eastern domain white-mica grains have a higher phengitic component than those from the Western domain, consistent with Si content differences.

FIGURE 5 White-mica microstructures from the Porto Murtinho Complex (a–c), Caracol Complex (d), and Alto Tererê Formation (e); (f) white-mica chemistry variation across the Western and Eastern domains of the RAT based on the Tschermak substitution $[Al^{(vi)}+Al^{(iv)} \leftarrow \rightarrow (Fe+Mg+Mn)^{(vi)}+Si^{(iv)}]$ [Colour figure can be viewed at wileyonlinelibrary.com]

4.3 | Garnet chemistry and phase-equilibria modelling

The RAT lacks abundant rock units suitable for phase-equilibria modelling given the dominance of meta-

igneous felsic rock units with simple mineralogy (quartz +plagioclase+K-feldspar and mica). Nevertheless, we selected one key metasedimentary rock sample of the Alto Tererê Formation (FMR99) within close proximity to the Aldeia Tomázia Thrust Fault (Figure 2a). This

sample corresponds to a biotite-muscovite schist with low abundance of garnet porphyroblasts (<1%), typically with a well-defined S-C fabric indicating clockwise shear sense. Alkali-feldspar, plagioclase, and titanite are also present in the matrix, although titanite has low abundance and small grain-size (<10 μm). Chemical maps and profiles from the biggest garnet porphyroblast (∼300 μm diameter; Figure 4k,l) define three compositional zones, well highlighted by all end-members (grossular-X_{Grs}, almandine-X_{Alm}, spessartine-X_{Sps}, and pyrope-X_{Prp}) (Figure 6a). The core is dominated by X_{Grs} (0.330 ± 0.012 mole fraction) and X_{Sps} (0.417 ± 0.018) with lower X_{Alm} (0.247 ± 0.014) and X_{Prp} content (0.007 ± 0.012). The core–rim boundary is irregular, sinuous, and chemically marked by a sharp X_{Grs} and X_{Sps} decrease to 0.225 ± 0.017 and 0.395 ± 0.013, respectively, and greater increase of X_{Alm} (0.343 ± 0.011) and X_{Prp} content (0.038 ± 0.009). A small decrease in X_{Grs} (∼0.246 to 0.200) and slight increase in the remaining end-members in close contact to quartz inclusions in both core and rim are perceptible. The outer rim is the narrowest domain (<50 μm) with a straight to slightly sinuous rim–outer rim boundary. This transition is also marked by a sharp X_{Grs} increase (0.342 ± 0.032) and decrease of the remaining end-members. White-mica is characterized by high Al and Si content spanning 2.05–2.15 and 3.37–3.41 (p.f.u.), akin to the phengite series, and the biotite by X_{Mg} and Ti (p.f.u) average contents of 0.500 ± 0.008 and 0.084 ± 0.004 (Figure 6b).

The phase-equilibrium diagram was calculated for 450–650°C and 5.0–15.0 kbar (Figure 6c). Despite the zoned garnet porphyroblast and the low abundance of garnet-forming components (e.g., MnO), fractional crystallization might be negligible and was not considered given the garnet very low garnet abundance (<0.5% as confirmed by the modelling results) (Lanari & Engi, 2017). The model predicts the observed mineral assemblage at conditions of ∼470–650°C and ∼7.5–15 kbar. Isopleths of X_{Sps}, X_{Alm}, and X_{Grs} with respective relative uncertainties derived from the EPMA uncertainties (e.g., Lanari & Engi, 2017) indicate that the garnet core crystallized at P–T fields of ∼530–550°C and ∼9.7–10.4 kbar within the titanite stability field, whereas the rim crystallized at ∼580–600°C and 9.5–10.4 kbar in the transition between the titanite and rutile stability fields. The transition from the rim to the outer rim is accompanied by an increase in pressure under decreasing temperature, reaching P–T conditions of ∼560–580°C and 10.9–11.7 kbar. Both absolute and relative values and uncertainties are considered robust given that modification factors such as effect bulk composition fractionation might be negligible as previously mentioned (cf. Lanari & Duesterhoeft, 2019; Lanari & Engi, 2017). The Si (p.f.u)

content in white-mica spanning 3.37–3.41 defines a P–T field mostly consistent with the outer rim crystallization conditions.

4.4 | Apatite, titanite, and rutile U–Pb ages and trace element composition

4.4.1 | Porto Murtinho Complex (Western domain)

Three key samples from the Porto Murtinho Complex with distinct structural settings were selected for apatite and titanite U–Pb geochronology and trace element analyses (Figure 2). Apatite from sample FMR104 presents two chemically different groups. The dominant apatite (Group 1) has higher total REE content of 1,343 ± 374 ppm (average ± standard deviation) and median of 1,390 ppm, concave REE-chondrite normalized (reference values from McDonough & Sun, 1995) profiles with MREE enrichment (Figure 7a, black profiles). It presents $(La/Sm)_N$ and $(Gd/Yb)_N$ ratios of 1.30–0.16 and 4.54–0.77, respectively, and pronounced negative Sr and Eu anomalies with Eu/Eu* values of 0.23–0.09. Group 2 has lower total REE content (225 ± 41 ppm, median of 220 ppm) and HREE enrichment with $(La/Sm)_N$ and $(Gd/Yb)_N$ ratios spanning 0.37–0.18 and 0.92–0.68, respectively, with a pronounced Eu anomaly (Eu/Eu* ranging between 0.23 and 0.19) (Figure 7a, blue profiles). These apatite grains define a chemical trend ranging from high- to low-grade metamorphic apatite (Figure 7b). Despite classified into two groups, these apatite grains define a single inverse isochron in the Tera-Wasserburg diagram yielding a lower intercept age of 1,769 ± 38 Ma (2σ, MSWD = 2.1) (Figure 7c).

Apatite from sample FMR101 defines a chemically coherent group with total REE content of 3,457 ± 795 ppm (median of 3,596 ppm), fractionated chondrite-normalized REE profiles with LREE enrichment as indicated by the $(La/Yb)_N$ ratio spanning 15.65–1.35, and negative Sr and Eu anomalies with Eu/Eu* ranging from 0.79 to 0.45 (Figure 7d). This apatite set is akin to I-type and mafic-type apatite (Figure 7e), defining a single inverse isochron in the Tera-Wasserburg diagram yielding a lower intercept age of 1,782 ± 57 Ma (MSWD = 1.4; Figure 7f). This age is consistent with that obtained for sample FMR104 within error. Titanite from sample FMR101 also defines a chemically coherent group with total REE content of 16,452 ± 3,606 ppm (median of 16,800 ppm), LREE enrichment with $(La/Yb)_N$ between 7.73 and 1.25, and negative Eu anomaly with Eu/Eu* spanning 1.06–0.32 (Figure 7g). This titanite set defines a
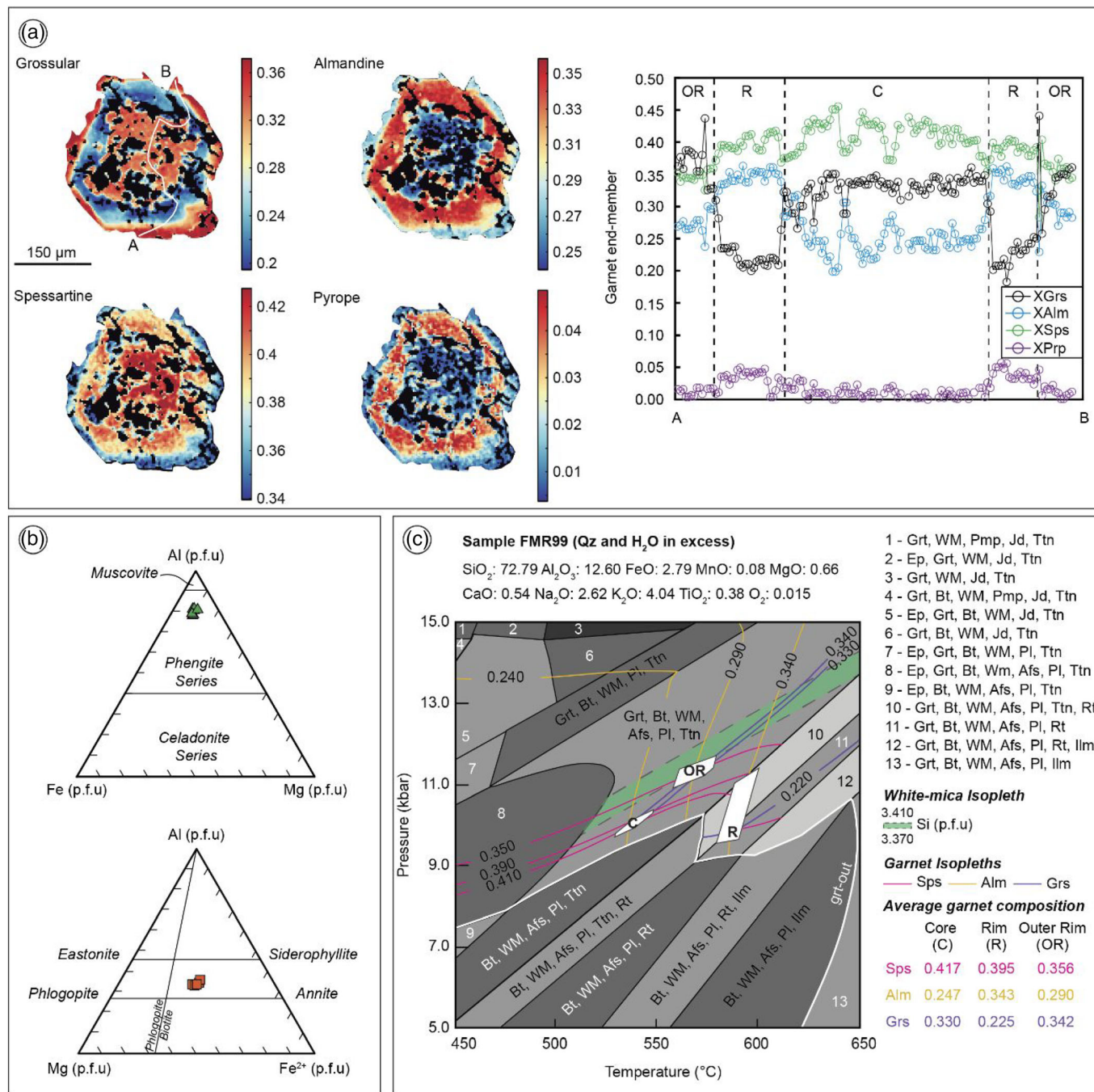
FIGURE 6 (a) Garnet composition maps and chemical profiles from sample FMR99; (b) ternary diagrams of the chemical composition of white-mica and biotite; (c) phase-equilibrium diagram for sample FMR99 with *P–T* fields constrained by isopleths of garnet end-members (Sps, spessartine; Alm, almandine; and Grs, grossular) and associated uncertainties extracted from the XMapTools (see Supporting Information S1 for EPMA data). Abbreviations for garnet zones are core, C; rim, R; outer rim, OR [Colour figure can be viewed at wileyonlinelibrary.com]

single inverse isochron in the Tera-Wasserburg diagram yielding a lower intercept age of $1,940 \pm 17$ Ma (MSWD = 1.3; Figure 7h). A subset of five U–Pb data with maximum $\pm 5\%$ discordance defines a concordia age of $1,959 \pm 25$ Ma (MSWD = 1.4; Figure 7i). The titanite age is consistent with the zircon U–Pb age of $1,947 \pm 9$ Ma for this sample (Faleiros et al., 2016).

Apatite from sample FMR109 defines a chemically coherent group with total REE content of $2,906 \pm 700$ ppm (median of 2,648 ppm), concave REE-chondrite normalized profiles with MREE dominance (Figure 7j). The $(La/Sm)_N$ and $(Gd/Yb)_N$ ratios span 0.60–0.33 and 2.02–1.26, respectively, and the REE-chondrite normalized profiles present pronounced negative Sr and
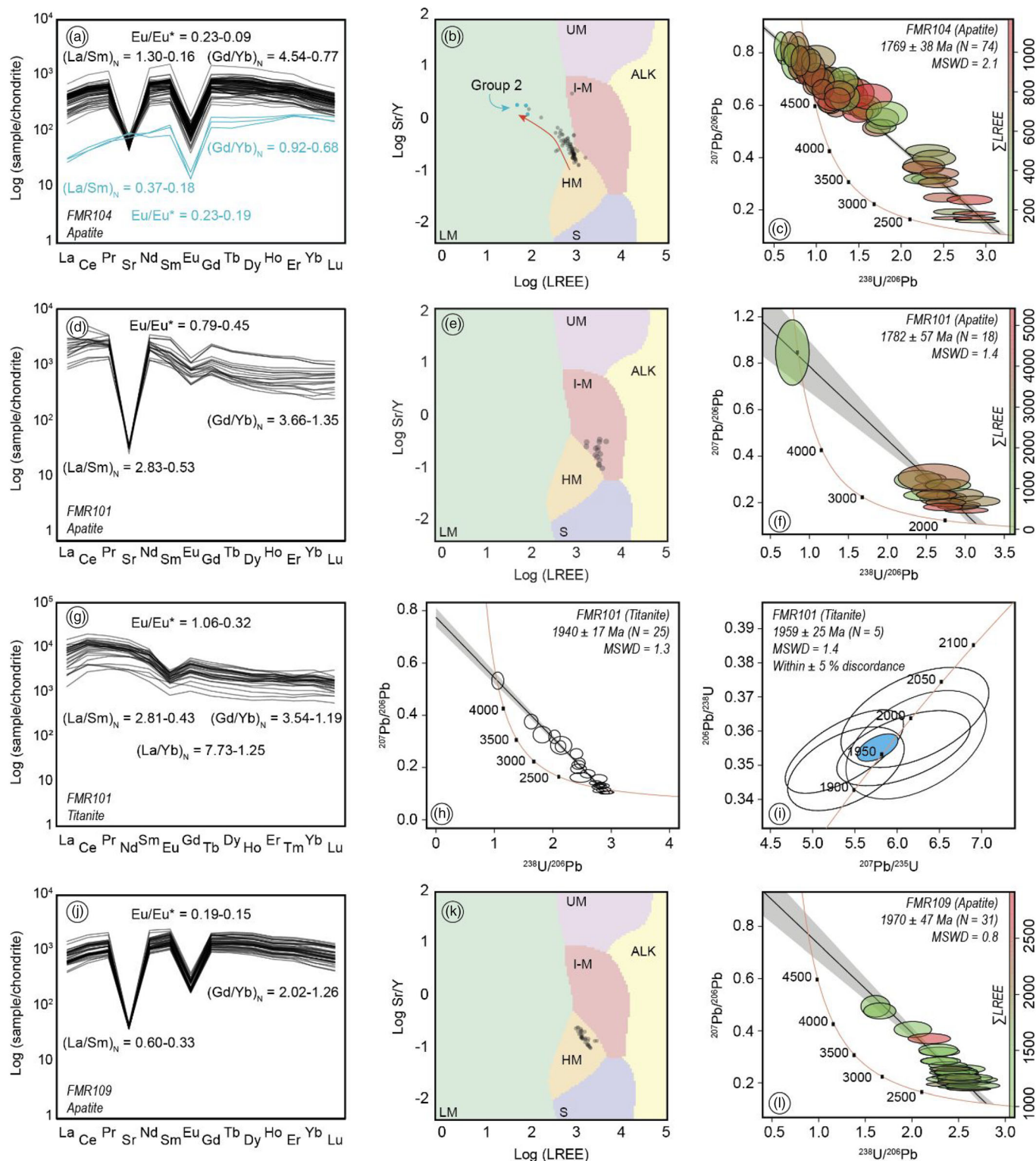
FIGURE 7 Apatite and titanite U–Pb–REE from key samples of the Porto Murtinho Complex. REE-chondrite normalized diagrams (a, d, g, j) were calculated using reference values from McDonough and Sun (1995) and apatite classification diagrams (b, e, h) follow O'Sullivan et al. (2020). Ellipse uncertainties are 2σ and errors are studentized at 95% confidence with no common-Pb correction applied. The colour-coded ellipsis represents to the sum of light rare earth element ($\sum$LREE = La+Ce+Pr+Sm) for each analysed grain. The abbreviations in the apatite classification diagrams stand to ALK, alkali-rich igneous rocks; HM, partial-melts/leucosomes/high-grade metamorphism; I+M, mafic I-type granitoids and mafic igneous rocks; LM, low- and medium-grade metamorphic and metasomatism; S, S-type granitoids and magmatic rocks with high aluminium saturation index; UM, ultramafic rocks including carbonatites, lherzolites, and pyroxenites [Colour figure can be viewed at wileyonlinelibrary.com]

Eu anomalies with Eu/Eu* between 0.19 and 0.15. This apatite set is akin to high-grade metamorphic apatite (Figure 7k), defining a single inverse isochron in the Tera-Wasserburg diagram yielding a lower intercept age of 1,970 ± 47 Ma (MSWD = 0.8; Figure 7l).

4.4.2 | Caracol Complex (Eastern domain)

Apatite from sample FMR147 has variable REE contents of 384 ± 336 ppm (median of 197 ppm), positive LREE, and mostly flat HREE trends, as indicated by the $(La/Sm)_N$ and $(Gd/Yb)_N$ spanning 0.96–0.06 and 2.01–0.68, respectively (Figure 8a). This apatite set has negative Sr and Eu anomalies with Eu/Eu* spanning 0.35–0.23. The majority of the apatite is akin to low- to medium-grade metamorphic apatite (Figure 8b), defining a single inverse isochron in the Tera-Wasserburg diagram yielding a lower intercept age of 1,409 ± 38 Ma (MSWD = 1.5; Figure 8c).

Apatite from sample FMR42 defines two chemically distinct groups on the basis of REE content and Sr anomalies. Group 1 has a lower total REE content of 113 ± 36 ppm (median of 108 ppm) and steep HREE fractionation as indicated by the $(La/Sm)_N$ and $(Gd/Yb)_N$ ratios spanning 1.73–0.30 and 0.20–0.13, respectively, and a positive Sr anomaly (Figure 8d). Group 2 has higher REE content of 406 ± 254 ppm (median of 259 ppm), steeper HREE fractionation with $(La/Sm)_N$ and $(Gd/Yb)_N$ ratios spanning 4.66–0.08 and 0.95–0.11, respectively, and a negative Sr anomaly. Both groups present negative Eu anomalies with similar Eu/Eu* ratios between 0.82 and 0.23. Despite chemically distinct, apatite grains from both groups are akin to low- to medium-grade metamorphic apatite (Figure 8e), defining a single inverse isochron in the Tera-Wasserburg diagram yielding a lower intercept age of 1,416 ± 70 Ma (MSWD = 1.7; Figure 8f). Titanite from sample FMR42 exhibits patchy zoning with bright and dark zones, or lacking clear zoning (Figure 4g,h inset). Overall, all titanite grains have similar REE-chondrite normalized profiles with strong HREE enrichment with $(La/Yb)_N$ spanning 0.04–0.01 and a subtle negative Eu anomaly with Eu/Eu* spanning 0.87–0.30. Chemical differences arise from the REE content with bright and dark zones having 538 ± 144 ppm (median of 543 ppm) and 381 ± 72 ppm (median of 390 ppm), whereas the titanite with undefined zoning has a REE content of 402 ± 105 ppm (median of 362 ppm). Despite the REE content differences, the three titanite groups define a single inverse isochron in the Tera-Wasserburg diagram yielding a lower intercept age of 1,243 ± 37 Ma (MSWD = 1.7; Figure 8i).

Rutile from two samples of the Caracol Complex were analysed for their U–Pb isotopic and trace element composition. Rutile grains from both samples are classified as niobian rutile with Nb/Ta ratios greater than 1 (Černý et al., 1964) and are characterized by high contents of high-field strength elements (HFSE) such as Nb, Ta, and W and U. A subset of 21 U–Pb data points out of 45 from sample FMR162 within maximum ±5% discordance yield a concordia age of 1,330 ± 8 Ma (MSWD = 2.4; Figure 8j) and average $^{207}Pb/^{206}Pb$ age of 1,382 ± 27 Ma (MSWD = 0.9). Similarly, 19 out of 30 U–Pb data points within maximum ±5% discordance from sample FMR140 yield a concordia age of 1,318 ± 9 Ma (MSWD = 2.4; Figure 8k) and average $^{207}Pb/^{206}Pb$ age of 1,354 ± 30 Ma (MSWD = 0.6; Figure 8l). Two concordant U–Pb analyses yield an older age of 1,629 ± 53 Ma (MSWD = 2.5). The average $^{207}Pb/^{206}Pb$ ages will be used for further interpretations given its lower dispersion. In summary, rutile from both samples yields consistent ages within uncertainty of 1,380–1,350 Ma.

4.5 | Garnet Lu–Hf ages

Two garnet-bearing rock samples of the Alto Tererê Formation were selected for garnet in situ Lu–Hf geochronology, mostly targeting the core of each analysed garnet. A total of 52 spot analyses were performed in garnet grains from sample FMR93. The data are characterized by $^{176}Lu/^{177}Hf$ and $^{176}Hf/^{177}Hf$ isotopic ratios spanning 0.3–4025.1 and 0.3–106.9, respectively, yielding an inverse isochron age of 1,334 ± 16 Ma (MSWD = 0.7) with initial $^{176}Hf/^{177}Hf$ of 0.2816 ± 0.0023 (Figure 9a). From sample FMR99, for which the P–T evolution was reconstructed, we measured Lu and Hf isotopes from 52 spot analyses. These garnet grains are characterized by $^{176}Lu/^{177}Hf$ and $^{176}Hf/^{177}Hf$ isotopic ratios spanning 0.03–24.18 and 0.28–0.92, respectively, yielding an inverse isochron age of 1,348 ± 24 Ma (MSWD = 0.6) with initial $^{176}Hf/^{177}Hf$ of 0.2823 ± 0.0015 (Figure 9b).

4.6 | White-mica Rb–Sr ages

4.6.1 | Porto Murtinho (Western domain)
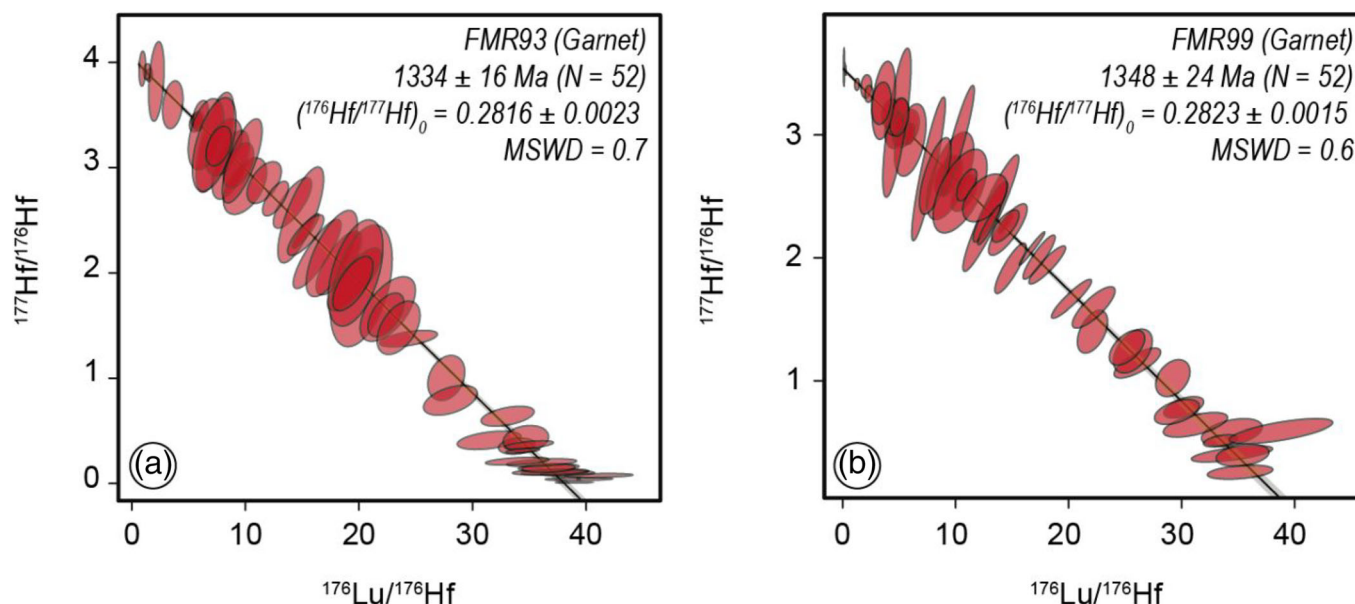
We collected Rb–Sr isotopes from 23 spot analyses on white-mica grains from sample FMR104, revealing $^{87}Rb/^{86}Sr$ and $^{87}S/^{86}Sr$ ratios of 12.3–59.4 and 1.0–2.2, respectively, and a plagioclase-anchored ($n = 7$ grains) isochron age of 1,778 ± 11 Ma (MSWD = 1.9; Figure 10a) with an initial $^{87}Sr/^{86}Sr$ intercept of 0.7068 ± 0.0015. Similarly, we collected Rb–Sr isotopes
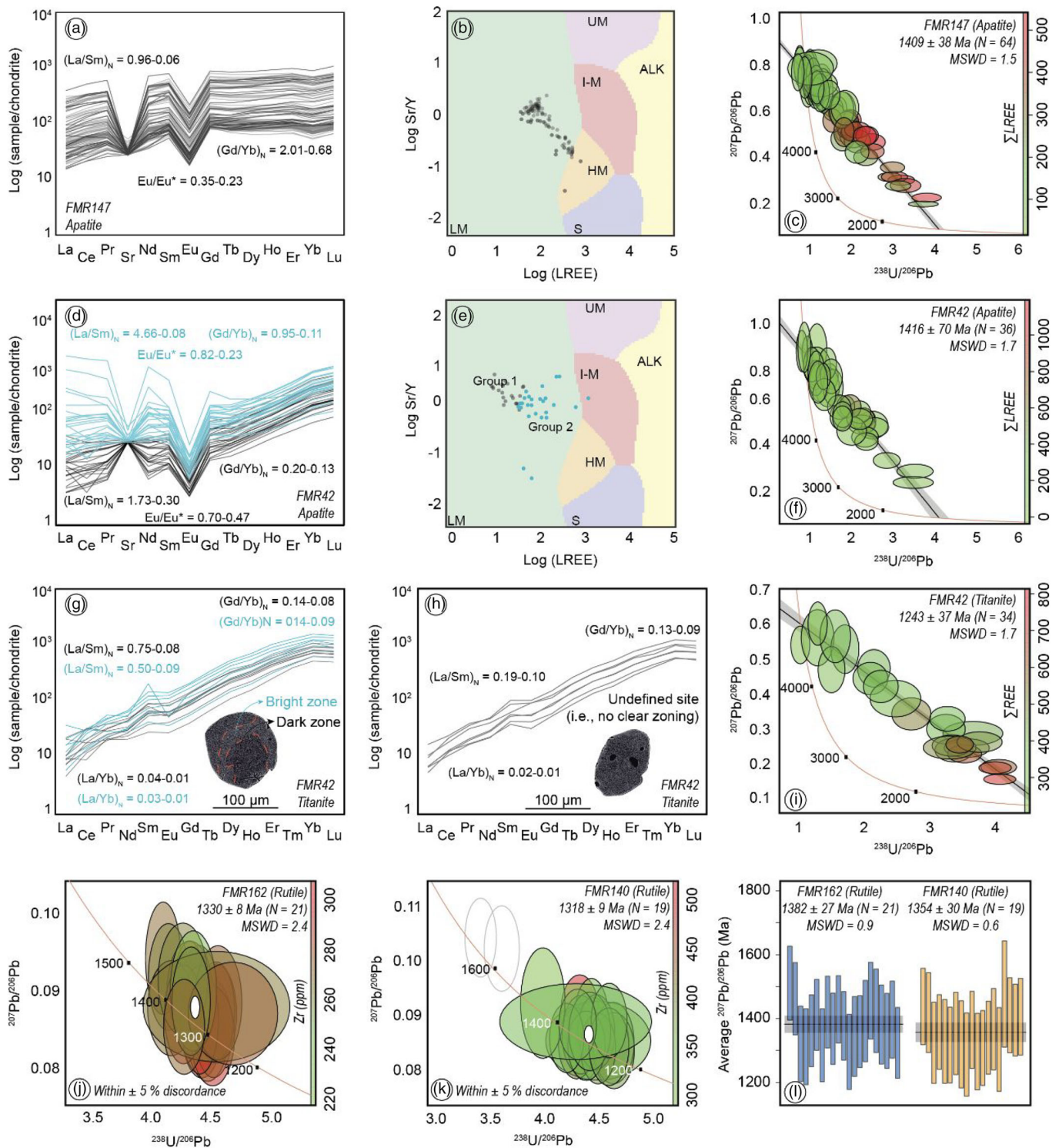
FIGURE 8 Apatite and titanite U–Pb–REE from key samples of the Caracol Complex. REE-chondrite normalized diagrams (a, d, g, h) were calculated using reference values from McDonough and Sun (1995) and apatite classification diagrams (b, e) follow O'Sullivan et al. (2020). Ellipse uncertainties are 2σ and errors are studentized at 95% confidence with no common-Pb correction applied. The colour-coded ellipsis represents to the sum of light rare earth element ($\sum$LREE = La+Ce+Pr+Sm) for each analysed grain. The abbreviations in the apatite classification diagrams stand to ALK, alkali-rich igneous rocks; HM, partial-melts/leucosomes/high-grade metamorphism; I+M, mafic I-type granitoids and mafic igneous rocks; LM, low- and medium-grade metamorphic and metasomatism; S, S-type granitoids and magmatic rocks with high aluminium saturation index; UM, ultramafic rocks including carbonatites, lherzolites, and pyroxenites [Colour figure can be viewed at wileyonlinelibrary.com]

FIGURE 9 Garnet Lu–Hf isochron ages from samples FMR93 (a) and FMR99 (b) of the Alto Tererê Formation. The data are plotted using an inverse diagram following Li and Vermeesch (2021). Ellipse uncertainties are 2σ and errors are studentized at 95% confidence [Colour figure can be viewed at wileyonlinelibrary.com]

from 24 spot analyses on white-mica grains from sample FMR105, exhibiting $^{87}Rb/^{86}Sr$ and $^{87}S/^{86}Sr$ ratios spanning 0.20–53.70 and 0.70–1.90, respectively. Fifteen Rb–Sr data define a principal isochron yielding a statistically reliable plagioclase-anchored ($n = 4$ grains) isochron age of 1,783 ± 19 Ma (MSWD = 1.0; Figure 10b) with an initial $^{87}Sr/^{86}Sr$ intercept of 0.7070 ± 0.0014. A secondary plagioclase-anchored isochron is defined by five white-mica Rb–Sr data, yielding a younger isochron age of 1,614 ± 28 Ma (MSWD = 1.1) with an initial $^{87}Sr/^{86}Sr$ intercept of 0.7085 ± 0.0018. From sample FMR109, we collected Rb–Sr isotopes from 25 spot analyses on white-mica grains, which indicate $^{87}Rb/^{86}Sr$ and $^{87}S/^{86}Sr$ ratios of 15.73–73.94 and 1.07–2.44, respectively. These grains define a statistically reliable plagioclase-anchored ($n = 9$ grains) isochron age of 1,629 ± 23 Ma (MSWD = 1.7) with an initial $^{87}Sr/^{86}Sr$ intercept of 0.7072 ± 0.0017.

In summary, white-mica grains from three samples of the Porto Murtinho Complex record two groups of isochron ages at *c.* 1,780 Ma and 1,625 Ma with similar initial $^{87}Sr/^{86}Sr$ intercept of 0.7073 ± 0.0012.

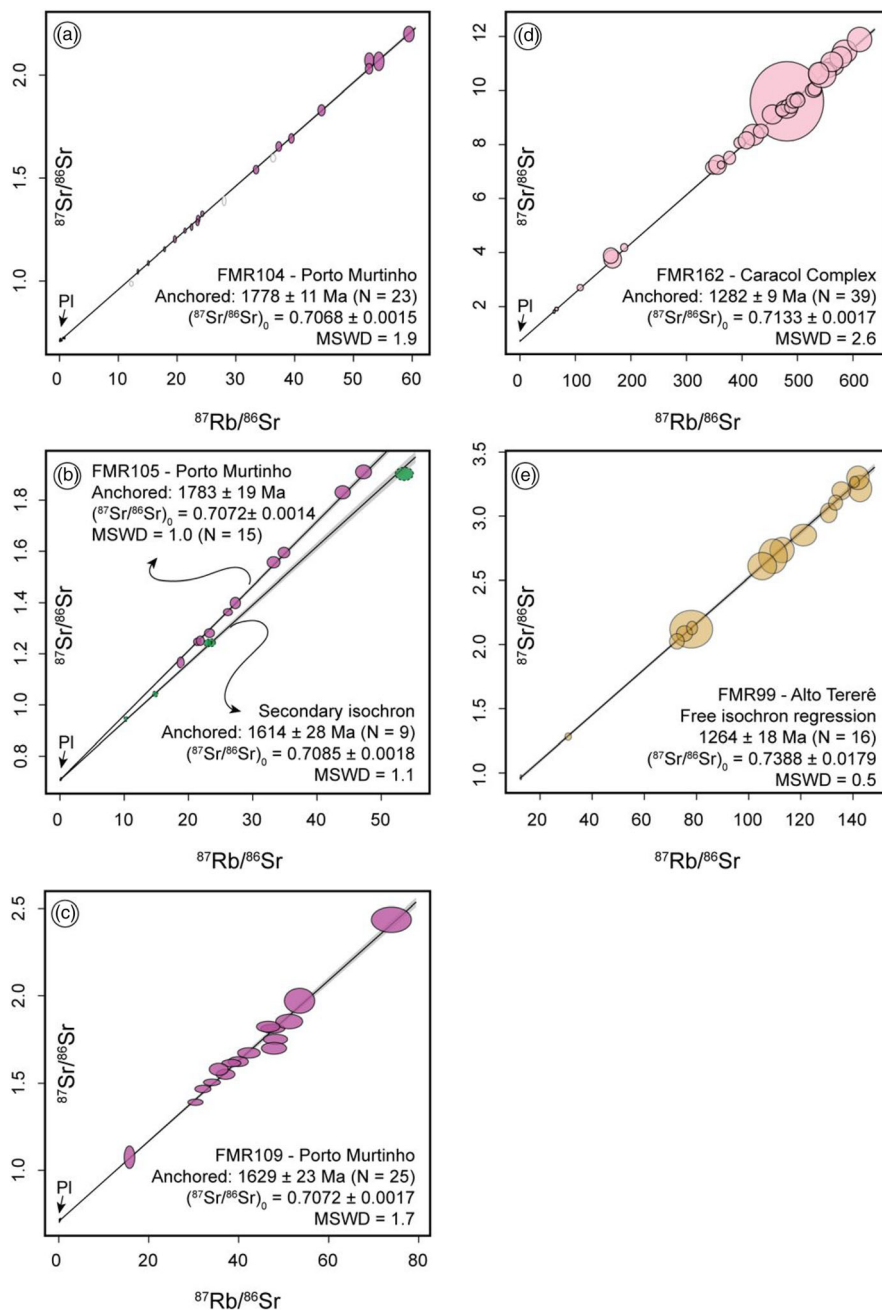### 4.6.2 | Caracol Complex and Alto Tererê Formation (Eastern domain)

We collected Rb–Sr isotopes from 33 spot analyses from sample FMR162 (Caracol Complex), indicating grains with highly variable $^{87}Rb/^{86}Sr$ and $^{87}S/^{86}Sr$ ratios spanning 61.5–612.0 and 1.8–11.9, respectively. The data

define a single isochron yielding a plagioclase-anchored ($n = 6$ grains) isochron age of 1,282 ± 9 Ma (MSWD = 2.6) with an initial $^{87}Sr/^{86}Sr$ intercept of 0.7133 ± 0.0017 (Figure 11d). From the metasedimentary rock sample FMR99 (Alto Tererê Formation), we collected Rb–Sr isotopes from 16 spot analyses, which also display highly variable $^{87}Rb/^{86}Sr$ and $^{87}S/^{86}Sr$ ratios spanning 12.7–142.7 and 0.9–3.3, respectively. They define a single isochron yielding a statistically reliable, free anchor isochron age of 1,264 ± 18 Ma (MSWD = 0.5; Figure 11e) with an initial $^{87}Sr/^{86}Sr$ intercept of 0.7388 ± 0.0179.

5 | DISCUSSION

5.1 | Nature and significance of crustal structures

The combination of airborne magnetic data with zircon U–Pb–Hf data from the main meta-igneous units from the RAT reveal the nature and significance of the structure between the Western and Eastern domains, currently known as the Aldeia Tomázia Shear Zone (Cordani et al., 2010; Faleiros et al., 2016). The smooth magnetic transition from high (Western domain) to low (Eastern domain) magnetic anomalies is consistent with a low-angle east dipping structure. Because the regional structural setting of the RAT is characterized by N-trending foliations dipping shallowly (20–30°) east and

FIGURE 10 White-mica Rb–Sr isochrons from the Porto Murtinho Complex (a–c), Caracol Complex (d), and Alto Tererê Formation (e). Isochron ages, number of spots, uncertainties, initial $^{87}Sr/^{86}Sr$ intercept, and MSWD are presented in the lower right corner. Ellipse uncertainties are 2σ and errors are studentized at 95% confidence [Colour figure can be viewed at wileyonlinelibrary. com]

shallowly E-plunging stretching lineation with top-to-west kinematic shear sense (Faleiros et al., 2014), we suggest that the Aldeia Tomázia Shear Zone represents a W-verging thrust fault. As such, we recommend modifying the name of this structure to the Aldeia Tomázia Thrust Fault hereafter to avoid misinterpretation.

Although the Aldeia Tomázia Thrust Fault clearly separates two different crustal domains (Figure 11), it might not correspond as a suture zone stricto sensu (e.g., Indus-Tsangpo suture zone; Honegger et al., 1982; Xu et al., 2015) as previously suggested and accepted since Cordani et al. (2010). Nevertheless, it is still an important feature in the RAT structural compartmentation. We envisage this structure may have a greater regional significance, requiring detailed investigations based on regional mapping and airborne magnetic surveys. The timing of this structure will be discussed below.

5.2 | Significance of accessory mineral composition and ages

Here we discuss the significance of the mineral geochemistry and ages. A quantitative comparison with trace element data from the literature was carried out using

FIGURE 11 Variation of magnetic signal and zircon εHf_T across the RAT (from Western to Eastern domain) highlighting the Aldeia Tomázia Thrust Fault as a major crustal boundary. Zircon εHf_T data were taken from Ribeiro, Cawood, et al. (2020) [Colour figure can be viewed at wileyonlinelibrary.com]
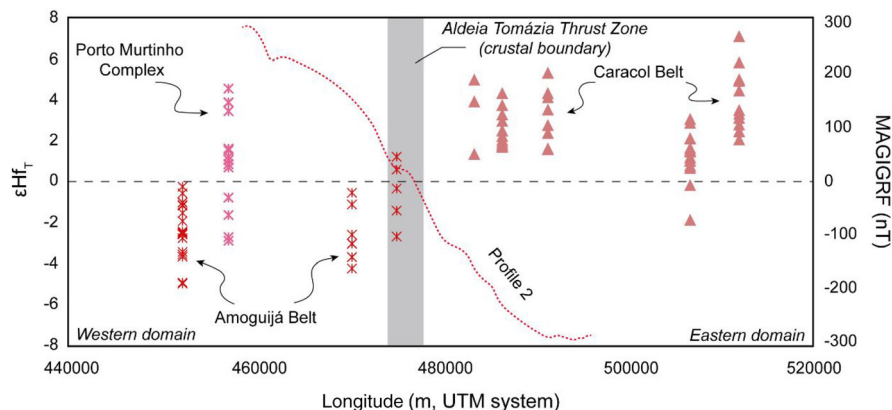
lambda coefficients (λ_n). These are shape coefficients that describe the chondrite-normalized patterns with λ_0 describing the average chondrite-normalized REE abundances, whereas λ_1 and λ_2 describing the linear slope and the quadratic curvature, respectively (O'Neill, 2016). The lambda coefficients were calculated with the online BLambaR calculator (Anenburg, 2020) (https://lambdar.rses. anu.edu.au/blambdar/). All trace element data were normalized to the chondrite reference values from McDonough and Sun (1995).

5.2.1 | Apatite

Apatite from the Porto Murtinho and Caracol complexes have different trace element chemistries and U–Pb ages. In general, the higher REE content, negative Sr and Eu anomalies, and enrichment of LREE–MREE characteristics of apatite from the Porto Murtinho Complex are akin to igneous apatite (Belousova et al., 2001; Ribeiro, Mulder, et al., 2020; Sha & Chappell, 1999). However, when the compositions are plotted in the apatite classification diagram, only apatite from sample FMR101 plots in the sections that correspond to I-type and mafic igneous rocks (O'Sullivan et al., 2020), whereas those from samples FMR104 and FMR109 plot as high-grade metamorphic apatite (Figure 12a). Because the high-grade metamorphic field was calibrated with rocks that may have experienced anatexis, this field could share chemical similarities with apatite from S-type granitoids leading to possible misclassification as discussed elsewhere (O'Sullivan et al., 2020, 2021). In fact, it has been statistically demonstrated that apatite from S-type granitoids is misclassified as high-grade metamorphic rocks 17% of the time, whereas apatite from high-grade metamorphic rocks was misclassified 33% of the time (O'Sullivan et al., 2020). Given the lack of evidence of high-grade metamorphic processes and that the Porto Murtinho Complex consists of S- and I-type granitoids (Faleiros et al., 2016), we interpret the apatite from the complex as

recording an original igneous signature. Group 2 apatite from sample FMR104, however, has a much lower REE content and significant LREE depletion and is classified as low- to medium-grade metamorphic apatite. These chemical signatures are similar to those of recrystallized apatite (Ribeiro, Lagoeiro, et al., 2020), possibly indicating chemical re-equilibration during medium-grade deformation and metasomatism (Glorie et al., 2019; Odlum & Stockli, 2020; Ribeiro, Lagoeiro, et al., 2020).

Apatite from sample FMR109 still preserves the original igneous chemistry and U–Pb age (1,970 ± 47 Ma) overlapping with zircon U–Pb ages from the Porto Murtinho Complex (Faleiros et al., 2016; Ribeiro, Cawood, et al., 2020), whereas apatite from samples FMR104 and FMR101 are c. 200 Ma younger than the average crystallization age of the Porto Murtinho Complex. Because these samples are granitic mylonites and apatite has otherwise retained its igneous chemistry, we interpret that the apatite U–Pb system was reset via volume diffusion in response to a medium-grade mylonitization process (Jepson et al., 2021; Odlum & Stockli, 2020; Ribeiro, Mulder, et al., 2020). Thus, the c. 1,780 Ma age from apatite may reflect the cooling age at conditions of 450–550°C.

Apatite grains from the Caracol Complex show different chemical signatures compared with those from the Porto Murtinho Complex with the former having lower REE contents and fractionated REE-chondrite normalized profiles with HREE enrichment. These grains are predominantly classified as low- to medium-grade metamorphic apatite (Figure 12a), in agreement with chemical characteristics of metamorphic/metasomatic apatite (Glorie et al., 2019; Henrichs et al., 2019, 2018; Ribeiro, Lagoeiro, et al., 2020). Apatite from samples FMR147 and FMR42 record c. 400–350 Ma younger ages than the crystallization age of the Caracol Complex (Faleiros et al., 2016; Plens, 2018; Ribeiro, Cawood, et al., 2020; Teixeira et al., 2020). These apatite ages are interpreted to reflect (re)crystallization in response to a medium-grade metamorphic/metasomatic event affecting the Caracol Complex.
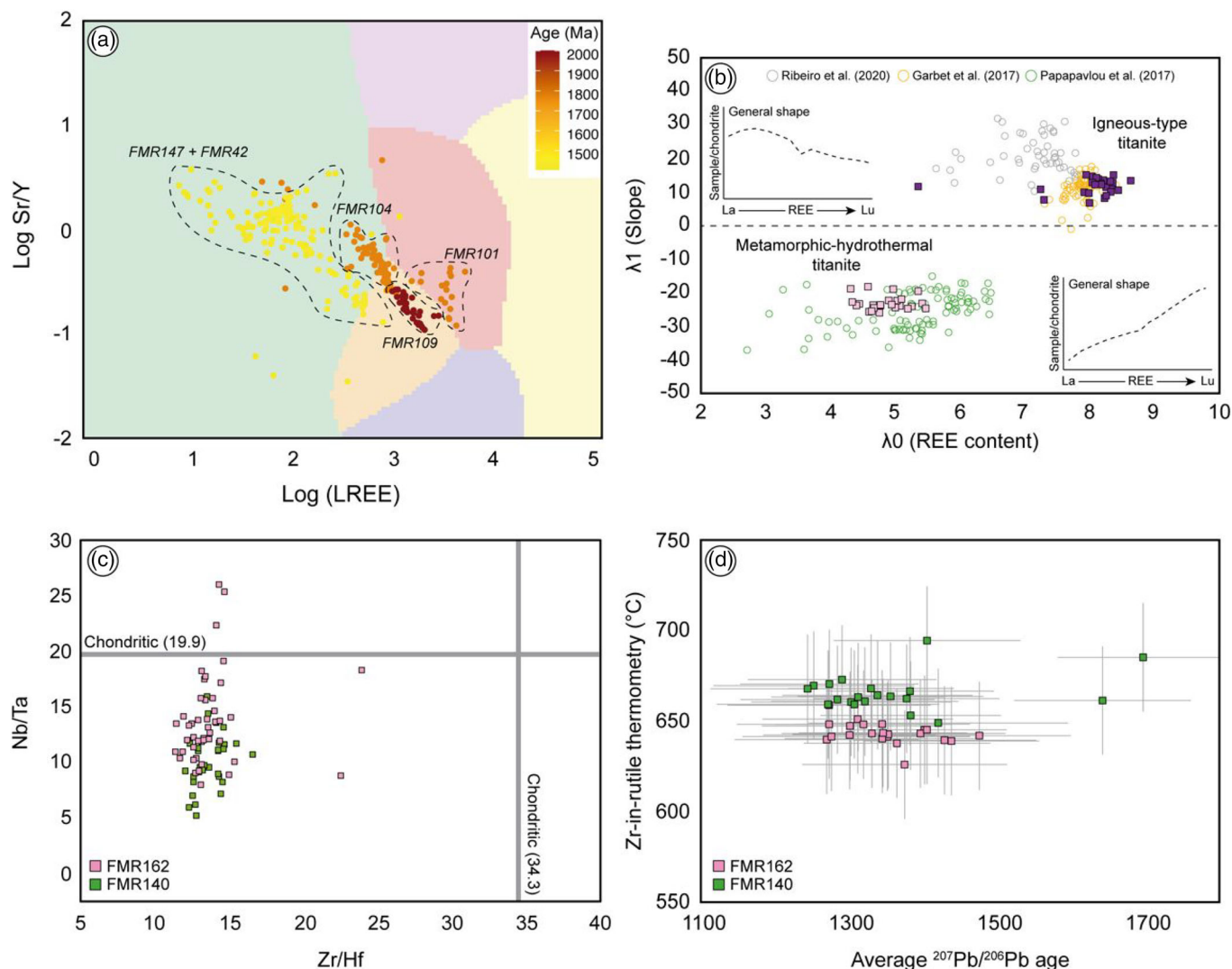
FIGURE 12 (a) Apatite classification diagram (O'Sullivan et al., 2020) with apatite data from all studied samples ranked by age (Ma); (b) chemical comparison between the titanite from the RAT (filled symbols) with others from the literature (hollow symbols). The reader is referred to O'Neill (2016) for detailed information about the lambda (λ_n) parameters; (c) Zr/Hf versus Nb/Ta diagram and (d) Zr-in-rutile thermometry (Tomkins et al., 2007) versus average $^{207}Pb/^{206}Pb$ rutile age from the Caracol Complex [Colour figure can be viewed at wileyonlinelibrary.com]

5.2.2 | Titanite

Titanite from the Porto Murtinho and the Caracol complexes record contrasting chemistry and U–Pb ages. The Palaeoproterozoic REE- and LREE-rich titanite from the Porto Murtinho Complex (sample FMR101) defines a chemically coherent group of igneous titanite, as demonstrated by their similarity to the trace element composition of igneous titanite from the literature (Figure 12b) (e.g., Garber et al., 2017; Ribeiro, Mulder, et al., 2020). The igneous origin is also supported by the overlap, within uncertainties, between the titanite age (1,959 ± 25 Ma) and the zircon crystallization age of 1,947 ± 9 Ma (Faleiros et al., 2016). Assuming an average pressure of 0.5 GPa (~13 km depth for a normal

continental crust) for granite crystallization, silica-saturated environment (silica activity $\alpha_{SiO2} = 1.0$), and a minimum TiO_2 activity of 0.5 typical of crustal rock in the absence of rutile (Hayden et al., 2008, and references therein), we infer that the titanite from the Porto Murtinho Complex crystallized at temperature conditions of ~760°C. This temperature range is consistent with crystallization conditions of igneous titanite (e.g., Garber et al., 2017).

The Mesoproterozoic REE-poor and LREE-depleted titanite from the Caracol Complex (sample FMR42) defines a chemically coherent group despite having a clear patchy zoning, suggestive of fluid-mediated growth and redistribution of major elements during recrystallization in an open system (Harlov et al., 2006; Villa &

Williams, 2013). REE and LREE depletion are indicated by the lower coefficients λ_0 (total REE content) and λ_1 (slope) (Figure 12b), respectively, demonstrating great similarity with (re)crystallized titanite during medium-grade metamorphism and hydrothermal titanite (e.g., Garber et al., 2017; Papapavlou et al., 2017). The REE content of titanite is controlled by the crystallization of cogenetic phases such as allanite, apatite, and epidote, mostly affecting the LREE contents (Garber et al., 2017). Titanite from sample FMR42 has a clear crystallization relationship with biotite, epidote, and zoisite/clinozoisite (Figure 4f), possibly causing the strong LREE depletion in titanite. Assuming an average pressure of 1.0 GPa (extrapolating the pressure conditions from the Alto Tererê Formation given its same tectono-context) and a silica-saturated environment ($\alpha_{SiO2} = 1.0$), the Zr-in-titanite thermometer yields a crystallization temperature of ~700°C for TiO$_2$ activity of 0.5 and 735°C for activity of 1.0 (in presence of rutile). This temperature range is inconsistent with medium-grade metamorphic and hydrothermal titanite (e.g., Kirkland et al., 2017), and the discrepancy between the high crystallization temperature and the medium-grade and hydrothermal chemistry suggests that the Zr content in titanite is in disequilibrium with its crystallization conditions (e.g., Cioffi et al., 2019; Kirkland et al., 2017). Moreover, titanite from sample FMR42 records a U–Pb age of 1,243 ± 37 Ma, whereas metamorphic apatite from the same sample was dated at 1,416 ± 70 Ma. The titanite U–Pb data also define a more radiogenic initial $^{207}Pb/^{206}Pb$ ratio (~0.65) than the apatite U–Pb data (~1.0), possibly suggesting that the titanite crystallized from a U-bearing precursor (most likely a rutile). Given the higher closure temperature of titanite (~700°C) compared with apatite (~450–500°C) (Oriolo et al., 2018, and references therein), titanite should record an older or similar age than apatite formed during the same event. Thus, a simple cooling history fails to explain the geochronological data, suggesting that the titanite is likely to be associated with hydrothermal influx during late-stage metamorphism (e.g., Kirkland et al., 2017). The petrographic relationship of titanite with biotite, epidote, and clinozoisite also supports its late-stage metamorphic crystallization (Figure 4f).

5.2.3 | Rutile

Rutile from two samples of the Caracol Complex yields ages at around *c.* 1,380–1,350 Ma, which are *c.* 400 Ma younger than the respective igneous crystallization age (zircon U–Pb ages; Ribeiro, Cawood, et al., 2020). This niobian rutile is inferred to have a metamorphic affinity (Fe >> 1,000 ppm; Zack et al., 2004) with predominant

subchondritic signatures in the Zr/Hf versus Nb/Ta diagram (Figure 12c). Although rutile with high HFSE concentration was previously associated with pegmatite (Černý et al., 1999), aplitic granite (Michailidis, 1997), peraluminous granite (Carruzzo et al., 2006), and kimberlite (Tollo & Haggerty, 1987), Nb-Ta–Cr-rich rutile has also been associated with metasomatism and H$_2$O-oversaturated environments (Carruzzo et al., 2006; Tollo & Haggerty, 1987). Given the textural observations with rutile entrapped along quartz grain boundaries associated with several fluid inclusion trails (Figure 4g), a metasomatic origin is more plausible. Although considered as conservative elements, HFSE mobility can occur in a wide range of *P–T* conditions and particularly in high-pH environments, promoted by F-rich fluids (Jiang et al., 2005). The high F content of white-mica between 0.65% and 0.04% from sample FMR162 supports the presence of F-rich fluids and a metasomatic origin of rutile. HFSE-enriched rutile has been an important pathfinder for ore deposits across different tectonic settings (Porter et al., 2020; Rezvukhina et al., 2021; Scott et al., 2011; Scott & French, 2005; Tollo & Haggerty, 1987), and the presence of this HFSE-enriched niobian rutile in two samples of the Caracol Complex is promising for tracking potential deposits of critical metals (e.g., Nb and Ta).

The rutile crystallization temperature calculated with the Zr-in-rutile thermometer (calibrated for α-quartz stability field; Tomkins et al., 2007) using an average pressure of 1.0 GPa (extrapolating the pressure conditions from the Alto Tererê Formation) yields ~640°C and ~665°C for samples FMR162 and FMR140 (Figure 12d), respectively. Given that metasomatic rutile is likely to have crystallized at temperatures below ~450°C (Putnis, 1978; Putnis & Wilson, 1978), we suggest that the Zr content is in disequilibrium with the rock–fluid interaction, possibly due to the high Zr partition coefficient between rutile and aqueous fluid (Brenan et al., 1994), leading to Zr enrichment and an overestimation of crystallization temperatures. The lack of coeval zircon–rutile crystallization is also an important factor, given this thermometer was calibrated with a quartz–zircon–rutile buffer. The similar rutile and apatite U–Pb ages from the Caracol Complex supports rutile crystallization at similar thermal conditions.

5.2.4 | White-mica

In situ Rb–Sr geochronology combined with textural and chemical constraints can resolve the timing of deformation and the role of fluids (Olierook et al., 2020; Van Daele et al., 2020). Coarse-grained white-mica from the NW-trending Porto Murtinho Complex (FMR104 and

FMR105) has microstructures indicating crystal-plastic deformation (Bell et al., 1986; Wilson & Bell, 1979) and lower phengite contents in comparison with white-mica from the Caracol Complex and Alto Tererê Formation (Figure 5f). The Porto Murtinho Complex white-mica grains show consistent initial $^{87}Sr/^{86}Sr$ and isochron ages of *c*. 1,780 Ma, in agreement with reset apatite U–Pb ages from the same complex (Figure 13). Given the similarity with apatite ages, the evidence of crystal-plastic deformation, and that the white-mica Rb–Sr isotopic system can be affected by medium-grade deformation (∼500–500°C; Eberlei et al., 2015; Inger et al., 1996; Oriolo et al., 2018, and references therein), we interpret the white-mica Rb–Sr isochron ages from the NW-trending Porto Murtinho

Complex as reset ages (i.e., due to diffusion) in response to deformation.

In contrast, white-mica grains from N-trending Porto Murtinho Complex (sample FMR109) define an isochron age of 1,629 ± 23 Ma (Figure 10c) that is significantly younger than the apatite age from the same sample, which dates the protolith's crystallization (1,970 ± 47 Ma; Figure 7l). A similar age is recorded in the few white-mica grains analysed from sample FMR105 (1,614 ± 28 Ma; Figure 10b). These younger ages, but with similar initial $^{87}Sr/^{86}Sr$ ratios to those from samples FMR104 and FMR105, may reflect a second thermal event that affected the Porto Murtinho Complex at *c*. 1,625 Ma at temperature conditions below apatite closure
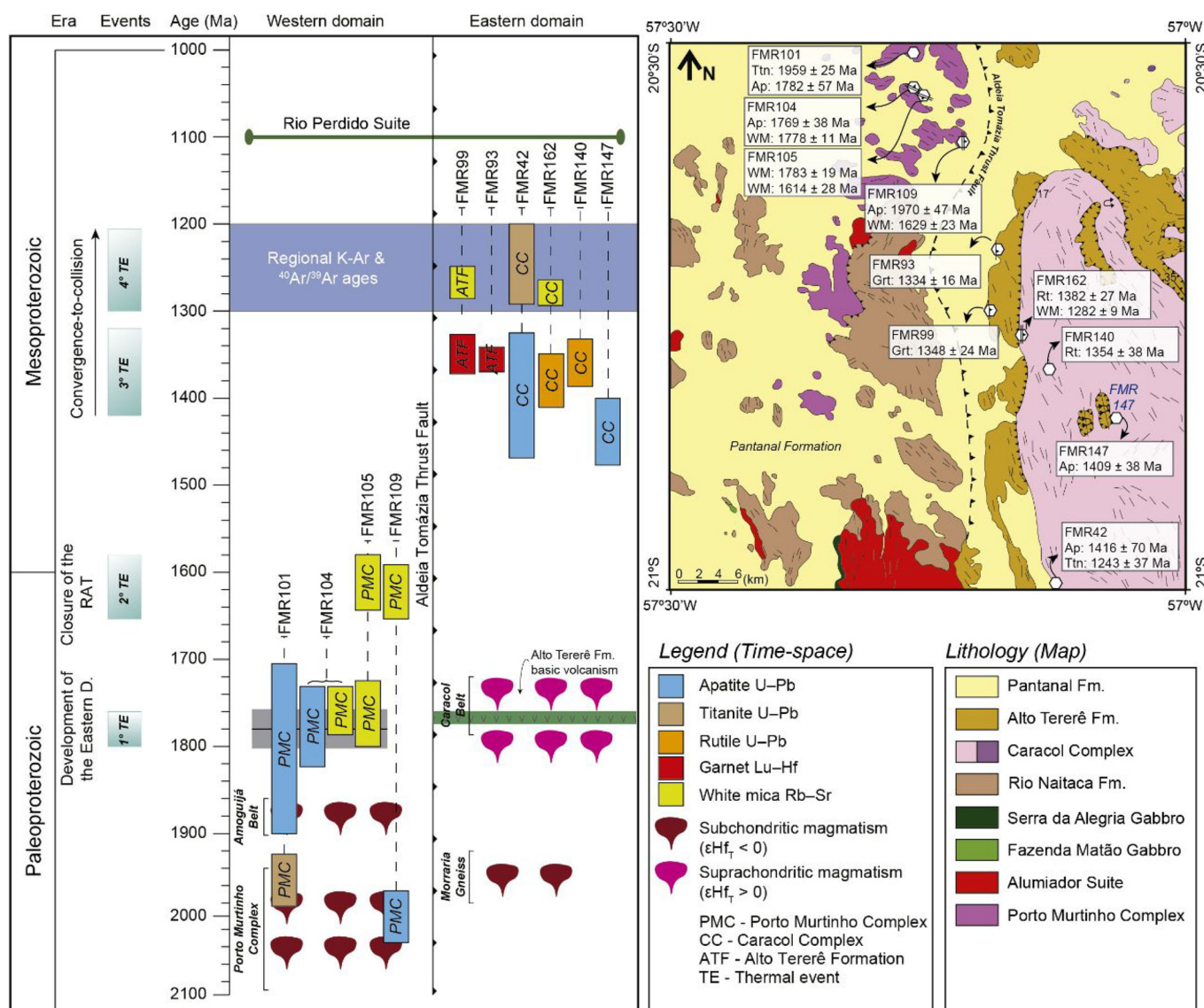
FIGURE 13 Time–space plot illustrating the distribution of multi-mineral ages across the RAT (adapted from Ribeiro, Cawood, et al., 2020). The geological map with location of analysed samples is located in the top right corner with the mineral ages obtained in this study. Samples are distributed in the time–space plot according to their geographic position in relation to the ATTF. Mineral abbreviations are Ap, apatite; Ttn, titanite; Rt, rutile; Grt, garnet; WM, white-mica [Colour figure can be viewed at wileyonlinelibrary.com]

temperature (∼450–550°C). This interpretation is supported by low temperature microstructures such as BLG recrystallization in quartz (280–400°C; Faleiros et al., 2010; Stipp et al., 2002a, 2002b).

White-mica from the Caracol Complex (FMR162) and the Alto Tererê Formation (FMR99) has high phengite content (higher Si p.f.u.) (Figure 5f) and an elongated shape defining the metamorphic foliation, and lack microstructures related to crystal-plastic deformation (Figure 5d,e). White-mica from both units yields similar Rb–Sr isochron ages of c. 1,280 Ma. These ages are within error of the late-stage titanite age (1,243 ± 37 Ma; FMR42) and significantly younger than the metamorphic apatite U–Pb ages (c. 1,410 Ma; FRM147, FMR42) from the Caracol Complex. Based on the white-mica microstructures and the similarity between the Rb–Sr isochron ages with the titanite U–Pb age, we interpret the white-mica Rb–Sr ages to represent (re)crystallization ages with Sr homogenization through fluid-mediated processes during deformation (Glodny et al., 2003; Hickman & Glassley, 1984). The high $^{87}Rb/^{86}Sr$ ratios and initial $^{87}Sr/^{86}Sr$ recorded by the Caracol Complex (0.7133) and the Alto Tererê Formation (0.7388) demonstrate greater affinity with crustal processes such as reworking during orogenic processes.

5.2.5 | Garnet

Garnet Lu–Hf ages from two samples of the Alto Tererê Formation agree within error, dating the garnet cores at c. 1,340 Ma. Additionally, phase-equilibria modelling combined with garnet in situ Lu–Hf geochronology from the metasedimentary rock sample FMR99 of the Alto Tererê Formation demonstrate for the first time the existence of a Mesoproterozoic high-pressure/medium temperature (HP/MT) metamorphic event (∼530–550°C and ∼9.7–10.4 kbar; Figure 6c) at 1,348 ± 24 Ma (Figure 9b). The garnet chemical zonation records an anticlockwise P–T path in the phase-equilibrium diagram (considering the simplest path), with isobaric heating (core to rim) followed by an increase in pressure under decreasing temperature (rim to outer rim) reaching conditions of ∼560–580°C and 10.9–11.7 kbar (Figure 6c). The Si isopleth in phengite (p.f.u.) are shown to be in equilibrium with the garnet outer rim, allowing indirect dating of the garnet outer rim with the phengite in situ Rb–Sr age of 1,264 ± 18 Ma (Figure 10e). Thus, we conclude that this records a metamorphic timespan of c. 110 Ma.

The garnet porphyroblast from FMR99 presents sharp chemical transitions between the three zones and a sinuous and irregular core–rim boundary, suggesting distinct episodes of garnet crystallization with core resorption

and low diffusion between zones (Giuntoli et al., 2018; Vho et al., 2020). This supports the interpretation of three distinct episodes of garnet growth, with the garnet core representing growth at c. 1,350 Ma and the outer rim growth at c. 1,260 Ma, both at HP/MT conditions. The first growth stage agrees with apatite and rutile U–Pb and white-mica Rb–Sr ages from the Eastern domain of the RAT (Figure 13), and the latter agrees with the late-stage metamorphic titanite U–Pb age from the Eastern domain and with regional K-Ar and $^{40}Ar/^{39}Ar$ ages from across the RAT (Araújo et al., 1982; Cordani et al., 2010; Lacerda Filho et al., 2020).

5.3 | Thermal events

Our petrochronology data across a suite of mineral phases along with previous published ages enable the recognition of a series of tectonothermal events in the RAT (Figure 13).

5.3.1 | 1,780 Ma

The Porto Murtinho Complex exposed in the northern domain of the study area exhibits a unique NW-trending vertical mylonitic foliation in the RAT (samples FMR101, FMR104, and FMR105). For the first time, apatite U–Pb and white-mica Rb–Sr ages document the existence of a deformation event at c. 1,780 Ma, responsible for the development of the NW-trending mylonitic fabric (Figure 13). Because titanite from one sample retains the protolith age (1959 ± 25 Ma, FMR101), we infer that this deformational event occurred at temperatures lower than that of average Pb closure in titanite (∼600–700°C), and higher than the average Pb closure temperature of apatite (∼450–550°C) (Chamberlain & Bowring, 2000; Cherniak, 2010; Oriolo et al., 2018; Schoene & Bowring, 2006). We infer that this deformational event occurred at temperatures of ∼450–550°C, consistent with reset of the apatite U–Pb and white-mica Rb–Sr systems (e.g., Eberlei et al., 2015; Jepson et al., 2021; Kirkland et al., 2017; Odlum & Stockli, 2020; Olierook et al., 2020; Ribeiro, Mulder, et al., 2020). The deformation temperature is qualitatively supported by the dominance of quartz SGR and GBM (Figure 3a–d), commonly developed at medium-grade thermal conditions in strain rate regimes for natural faults (Faleiros et al., 2010; Stipp et al., 2002a, 2002b).

Close to the Aldeia Tomázia Thrust Fault, the mylonitic structure of the Porto Murtinho Complex changes from NW- to N-trending with decreasing dip, possibly suggesting a structural rotation related to an

active period of the Aldeia Tomázia Thrust Fault with a sinistral shearing component. However, apatite from this location records the crystallization age of the Porto Murtinho Complex (1970 ± 47 Ma, FMR109), indicating that neither the 1,780 Ma thermal event nor the structural overprint of the Aldeia Tomázia Thrust Fault affected the apatite U–Pb system. From this, we conclude that the c. 1,780 Ma deformation had a heterogeneous thermal impact possibly due to strain localization and shear heating in some domains of the Porto Murtinho Complex. Additionally, we infer that the structural influence of the Aldeia Tomázia Thrust Fault into the Porto Murtinho Complex occurred at temperatures below the apatite Pb closure temperature (∼450–550°C), consistent with the brittle microstructures recorded by sample FMR109 (Figure 3d).

5.3.2 | 1,625 Ma

White-mica grains from two samples of the Porto Murtinho Complex (FMR109 and FMR105) in the basement of the Western domain record a second thermal event at c. 1,625 Ma. Because apatite from sample FMR109 dates igneous crystallization and those from sample FMR105 date the c. 1,780 Ma event, we infer that the c. 1,625 Ma event occurred at temperatures below the apatite closure temperature, preventing it from being reset while resetting the white-mica Rb–Sr system. This interpretation is supported by low temperature microstructures including pervasive quartz BLG overprint and fractured feldspar (Figure 3d). Additionally, this suggests that the white-mica Rb–Sr system can be affected by thermal events with temperature conditions below ∼450°C (e.g., Olierook et al., 2020), pushing the lower limit of the closure temperature beyond what was previously suggested (<500°C; Eberlei et al., 2015).

Although it is clear that white-mica grains from the Porto Murtinho Complex were affected by the c. 1,780 and c. 1,625 Ma thermal events, it is difficult to clarify the origin of those grains. However, given the initial $^{87}Sr/^{86}Sr$ ratios among all analysed samples (∼0.707; Figure 10a–c) are similar to the average initial $^{87}Sr/^{86}Sr$ ratio from whole-rock determinations (Cordani et al., 2010) and the dominance of deformation-related microstructures (as opposed to recrystallization microstructures) (Figure 5), we speculate they all crystallized from the same source (potentially the protolith). Fluid influx could also promote reset of the white-mica Rb–Sr system, which could also explain the slightly different chemical composition of white-mica from sample FMR109 (Figure 5f). However, this is unlikely because the initial $^{87}Sr/^{86}Sr$ ratio for all samples of the Porto

Murtinho Complex is similar, and a new fluid influx would likely modify that ratio according to the fluid composition and source (Glodny et al., 2003).

5.3.3 | 1,420–1,340 Ma

The multi-mineral geochronology and phase-equilibria modelling demonstrate for the first time HP/MT metamorphism at c. 1420–1,340 Ma constrained by crystallization ages of metamorphic apatite, rutile, and garnet cores (Figure 13). This event is structurally related to the W-verging shortening that pervasively affected the RAT developing a hot-on-cold structure, typical of major thrust faults. The metamorphic constraints of this event indicate isobaric heating from ∼530°C to ∼590°C at around ∼10 kbar, resembling a convergent tectonic setting with thermal gradients of ∼53–59°C/GPa.

5.3.4 | 1,300–1,200 Ma event

Late-stage metamorphic titanite and syn-kinematic white-mica establish the last thermal event (Figure 13), in agreement with muscovite and biotite K–Ar and $^{40}Ar/^{39}Ar$ and a few monazite U–Pb ages (Araújo et al., 1982; Cordani et al., 2010; Lacerda Filho et al., 2016, 2020). This event has been used to infer the palaeogeographic proximity of the RAT and the SW Amazonian margin (Teixeira et al., 2020). The phase-equilibria modelling of the Alto Tererê Formation indicates an anticlockwise P–T path, with the garnet outer rim establishing a pressure increase possibly related to crustal thickening (e.g., Scodina et al., 2019).

5.4 | Tectonic significance

Prior to this study, the lack of thermal constraints for the tectono-metamorphic events in the RAT prevented accurate assessment of the timing of its consolidation into a single terrane and the relationship between the RAT and adjoining terranes (e.g., Paraguá Terrane and Amazonian Craton). We reveal four thermal events in the RAT and here we discuss their tectonic significance.

5.4.1 | Consolidation of the RAT

The Porto Murtinho Complex records for the first time two thermal events at c. 1,780 and c. 1,625 Ma. The first event is unlikely to represent the consolidation of the RAT, as its age is coeval with the magmatic evolution of

the Eastern domain between 1800 and 1,720 Ma (Figure 13). Based on this age similarity and the previous finding that the Western and Eastern domains of the RAT evolved in close spatial proximity (Ribeiro, Cawood, et al., 2020; Teixeira et al., 2020), we suggest that the Western and Eastern domains experienced a similar tectonic evolution at this time. In the Eastern domain, juvenile εHf_T input in zircon (Figure 1d) and basic magmatism with typical back-arc signatures at $1,768 \pm 6$ Ma (Lacerda Filho et al., 2016) suggest that the region was undergoing extension in an overall accretionary system (Ribeiro, Cawood, et al., 2020). The Morraria Gneiss (1,970–1,930 Ma; Cordani et al., 2010), recently interpreted to represent a fragment of the Porto Murtinho Complex in the Eastern domain (Ribeiro, Cawood, et al., 2020), may have rifted away from the Western domain during the c. 1,780 Ma extensional event. Detailed quantitative structural analyses to quantify the strain ellipse orientation and geometry are key to strengthening this hypothesis (Dewey et al., 1998; Launeau & Robin, 2005; Ribeiro et al., 2019).

The second thermal event at c. 1,625 Ma is preserved in a small domain of the Porto Murtinho Complex. The NW-trending mylonitic foliation of the Porto Murtinho Complex (dated at c. 1,780 Ma) is reorientated to a N-trend adjacent to the Aldeia Tomázia Thrust Fault (Figure 13, map inset). We interpret the NW- to N-trending structural reorientation of the Porto Murtinho Complex to be associated to the development of the ATTF at c. 1,625 Ma during the consolidation of the RAT as a single terrane. Because the c. 1,780 and c. 1,625 Ma events are uniquely recorded in the Porto Murtinho Complex and that the Amoguijá Belt of the Western terrane is mostly undeformed (Faleiros et al., 2016), we suggest that the Western domain was affected by thin-skin tectonics, whereas the Eastern domain was affected by thick-skin tectonics, with basement and supracrustal rocks intensely deformed and affected by amphibolite facies metamorphism, as previously envisaged in Faleiros et al. (2016).

In summary, combining the recent literature regarding the magmatic and crustal evolution of the RAT with the new thermal constrains presented here, we conclude that the RAT developed in a single accretionary system involving periods of advance and retreat spanning 2,100–1,840 and 1,800–1,720 Ma giving rise to the Western and Eastern domains (Faleiros et al., 2016; Ribeiro, Cawood, et al., 2020; Teixeira et al., 2020). The Eastern domain was juxtaposed with the Western domain along the Aldeia Tomázia Thrust Fault at c. 1,625 Ma, consolidating the RAT as a single crustal domain.

5.4.2 | Growing the SW Amazonian margin

The RAT was envisaged to represent a fragment of the Amazonia Craton in Cordani et al. (2010), a suggestion that was later reinforced by whole-rock Rb–Sr and zircon U–Pb-Hf isotopic data (Faleiros et al., 2016; Plens, 2018; Ribeiro, Cawood, et al., 2020; Teixeira et al., 2020). The RAT is currently separated from the SW Amazonian margin by the Paraguá Terrane and Neoproterozoic belts (e.g., Tucavaca Belt; Figure 1). The composite Paraguá Terrane has two domains (Paraguá and San Diablo) separated by a shear zone termed the San Diablo Front. Recent investigations in the San Diablo domain (southern domain of the Paraguá Terrane) have revealed the existence of Palaeoproterozoic meta-igneous rocks with whole-rock Sm–Nd and zircon U–Pb–Hf signatures similar to the Western domain of the RAT (Nedel, 2020; Nedel et al., 2021; Redes et al., 2020) (Figure 14a). The Chiquitania Group, a metasedimentary unit of the Paraguá Terrane intruded by the Lomas Maneches Suite, is characterized by detrital zircon U–Pb ages spanning 1910–1,690 Ma with a peak of c. 1,765 Ma (Boger et al., 2005). Based on multi-dimensional scaling analyses (performed in R following Vermeesch, 2013; Vermeesch et al., 2016), we demonstrate that the provenance of the Chiquitania Group is statistically comparable with those from the Alto Tererê Formation sourced from the Eastern domain of the RAT (Figure 14b). This statistical correlation is consistent with the proximity of the RAT and the Paraguá Terrane during the Palaeoproterozoic, and new detrital zircon U–Pb–Hf analyses of the Chiquitania Group could further evaluate this hypothesis.

Magmatism ceased at c. 1,700 in the RAT with final development of the Eastern domain (Caracol Complex) (Figure 14c), suggesting that subduction stopped or migrated elsewhere. While magmatism in the Paraguá Terrane is younger than that of the RAT (Figure 14c), the isotopic correlation between the RAT and the Paraguá Terrane suggests they evolved as a single accretionary orogenic system (Figure 14a). Thus, we envisage a possible migration of the magmatism towards the back-arc domain of the RAT (between the RAT and the SW Amazonian margin) during an advancing phase of the accretionary system (c. 1700–1,660 Ma; Boger et al., 2005). This hypothesis explains the magmatic lull in the RAT post c. 1,700 Ma and suggests a genetic correlation between the RAT and the Paraguá Terrane potentially in the same accretionary system. If this hypothesis is correct, the San Diablo domain is a plausible extension of the RAT to the north separated from the Paraguá Terrane by the San Diablo Front as previously suggested (Faleiros et al., 2016; Redes et al., 2015).
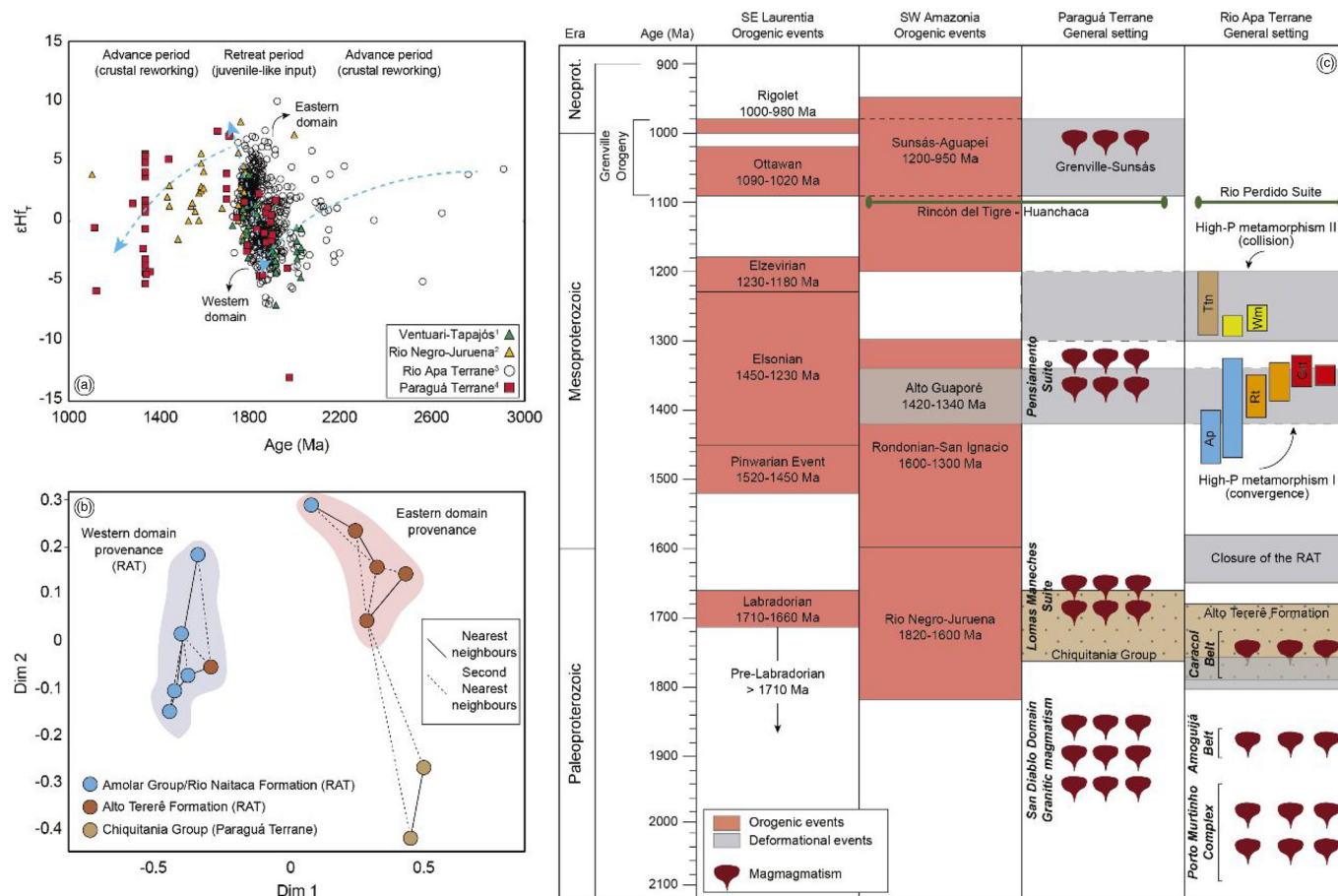
FIGURE 14 (a) Crystallization age (Ma) versus εHf_T from the Rio Apa and Paraguá terranes alongside data from the Ventuari-Tapajós and Rio Negro-Juruena from the Amazonian Craton (adapted from Ribeiro, Cawood, et al., 2020). Whole-rock εNd_T was converted to εHf_T following Vervoort et al. (2011); (b) multidimensional scaling diagram demonstrating the potential provenance of the Chiquitania Group (Paraguá Terrane) from the Eastern domain of the RAT (adapted from Ribeiro, Cawood, et al., 2020); (c) regional time–space plot including orogenic events and general settings of the SE Laurentia, SW Amazonia, Paraguá Terrane, and Rio Apa Terrane [Colour figure can be viewed at wileyonlinelibrary.com]

After the RAT consolidation, we interpret that the RAT was accreted to the Paraguá Terrane between 1,420 and 1,340 Ma during the Alto Guaporé orogeny (Rizzotto et al., 2013) (Figure 14c). This event is recorded in the Alto Tererê Formation as a HP/MT metamorphic event with garnet Lu–Hf age of $1,348 \pm 24$ Ma (FMR99; Figure 9b) as well as similar apatite and rutile U–Pb ages in the Caracol Complex (Figure 13) in association with W-verging thrust tectonics. Similar to the Palaeoproterozoic to Mesoproterozoic events in the RAT, SE Laurentia is characterized by long-lived subduction and protracted convergence prior to collision (Hynes & Rivers, 2010) with Mesoproterozoic events being characterized by continent–arc–continent collision and exhumation of high-pressure rocks (Carlson et al., 2007; Hynes & Rivers, 2010; Mosher et al., 2008). The similar tectono-magmatic history and the palaeogeographic reconstruction suggest a possible connection between SW Amazonian–SE Laurentia (Bispo-Santos et al., 2020; Evans, 2013; Johansson, 2009). Thus, the accretionary-to-collisional event recorded in the RAT (1,420–1,200 Ma) can be related to the Elsonian accretionary event in SE Laurentia, potentially recording the closure of the Mirovoi Ocean between SE Laurentia and SW Amazonia through two-sided subduction and suggesting a linked kinematic evolution of these cratonic masses at this time (Bettencourt et al., 2010; Cawood & Pisarevsky, 2017; Gower & Krogh, 2002; Hynes & Rivers, 2010; Rivers & Corrigan, 2000; Rizzotto et al., 2013; Sadowski & Bettencourt, 1996; Spencer et al., 2013).

The RAT-Paraguá mass collided with the SW Amazonian margin at 1,300–1,200 Ma, recorded in the Alto Tererê Formation as a HP/MT metamorphic event with an increase in pressure to ~11.5 kbar (Figure 6c) indicating crustal thickening typical of a collisional setting (e.g., Scodina et al., 2019). Given the evidence of a

Mesoproterozoic high-temperature metamorphic event in the Paraguá Terrane (Bettencourt et al., 2010, and references therein) and HP/MT metamorphic events in the RAT associated with this progressive convergence-to-collision tectonics, we suggest that the Paraguá Terrane and the RAT represent a paired metamorphic belt in the more general sense of Brown (2010), that is, the juxtaposition of penecontemporaneous belts with contrasting types of metamorphism and thermal gradients in response to plate tectonic processes.

6 | CONCLUSIONS

In this study, we have applied petrochronology to investigate the tectono-metamorphic evolution of the RAT and its significance for the evolution of the SW Amazonian margin during the Mesoproterozoic. We identified four tectono-metamorphic events: (i) c. 1,780 Ma recorded in the basement of the Western domain of the RAT related to the Eastern domain's development during a retreating episode of the accretionary orogenic system; (ii) c. 1,625 Ma corresponding with an important structural reorientation locally preserved in the Western domain of the RAT, establishing the consolidation of the RAT as a single crustal domain; (iii) c. 1,420–1,340 and c. 1,300–1,200 Ma ages are widespread in the Eastern domain and inferred to represent a progressive metamorphic event characterized by isobaric heating ($\sim$530°C to 600°C at $\sim$10 kbar) followed by an increase in pressure under decreasing temperature ($\sim$560–580°C and $\sim$10.9–11.7 kbar), establishing an anticlockwise P–T path related to a convergence-to-collision tectonics. The tectono-metamorphic evolution of the RAT broadly reflects that of the SW Amazonian margin during Rodinia assembly, in which the RAT was juxtaposed with the Paraguá Terrane at 1,420–1,340 Ma and collided with the SW Amazonian margin at 1,300–1,200 Ma, prior to Rodinia assembly. The timing of the Mesoproterozoic events along the Amazonian margin correlate with events along eastern Laurentia, with both characterized by a long-lived accretionary margin and overlapping tectonothermal events suggesting a linked kinematic evolution on opposing margins of the Mirovoi Ocean, perhaps due to closure across a double-sided subduction system (cf. Spencer et al., 2013).

This study highlights the importance of investigating tectono-metamorphic events in complex Precambrian terranes such as the Amazonian Craton and adjoining terranes by using multi-mineral petrochronology, including phase-equilibria modelling coupled to mineral chemistry and multi-mineral-methods geochronology with structural and microstructural controls. This approach allows determination of events that are generally missed by conventional regional zircon U–Pb and whole-rock isotopic analyses.

DATA AVAILABILITY STATEMENT
The data that support the findings of this study are available in the supporting information of this article.

ORCID
Bruno V. Ribeiro https://orcid.org/0000-0002-3652-1831
Melanie A. Finch https://orcid.org/0000-0001-9699-2769
Peter A. Cawood https://orcid.org/0000-0003-1200-3826
Frederico M. Faleiros https://orcid.org/0000-0003-2199-8116
Stijn Glorie https://orcid.org/0000-0002-3107-9028
Mahyra Tedeschi https://orcid.org/0000-0001-6573-0846
Robin Armit https://orcid.org/0000-0002-2843-8624
Vitor R. Barrote https://orcid.org/0000-0001-7442-9748

REFERENCES
Affonso, G. M. P. C., Rocha, M. P., Costa, I. S. L., Assumpção, M., Fuck, R. A., Albuquerque, D. F., Portner, D. E., Rodríguez, E. E., & Beck, S. L. (2021). Lithospheric architecture of the Paranapanema Block and adjacent nuclei using multiple-frequency P-wave seismic tomography. *Journal of Geophysical Research - Solid Earth*, *126*. https://doi.org/10.1029/2020JB021183

Aleinikoff, J. N., Schenck, W. S., Plank, M. O., Srogi, L., Fanning, C. M., Kamo, S. L., & Bosbyshell, H. (2006). Deciphering igneous and metamorphic events in high-grade rocks of the Wilmington Complex, Delaware: Morphology, cathodoluminescence and backscattered electron zoning, and SHRIMP U-Pb geochronology of zircon and monazite. *Geological Society of America Bulletin*, *118*, 39–64. https://doi.org/10.1130/B25659.1

Aleinikoff, J. N., Wintsch, R. P., Tollo, R. P., Unruh, D. M., Fanning, C. M., & Schmitz, M. D. (2007). Ages and origins of rocks of the Killingworth dome, south-central Connecticut: Implications for the tectonic evolution of southern New

England. *American Journal of Science*, *307*, 63–118. https://doi. org/10.2475/01.2007.04

Alves, A., de Assis Janasi, V., Neto, M. D. C. C., Heaman, L., & Simonetti, A. (2013). U–Pb geochronology of the granite magmatism in the Embu Terrane: Implications for the evolution of the Central Ribeira Belt, SE Brazil. *Precambrian Research*, *230*, 1–12. https://doi.org/10.1016/j.precamres.2013. 01.018

Anenburg, M. (2020). Rare earth mineral diversity controlled by REE pattern shapes. *Mineralogical Magazine*, *84*, 629–639. https://doi.org/10.1180/mgm.2020.70

Araújo, H. J. T., Santos Neto, A., Trindade, C. A. H., Pinto, J. C. A., Montalvão, R. M. G., Dourado, T. D. C., Palmeira, R. C. B., & Tassinari, C. C. G. (1982). Folha SF. 21—Campo Grande: geologia, geomorfologia, pedologia, vegetação e uso potencial da terra. In *Levantamento de Recursos Naturais* (Vol. 28, p. 416). DNPM, Projeto Radam Brasil.

Axelsson, E., Pape, J., Berndt, J., Corfu, F., Mezger, K., & Raith, M. M. (2018). Rutile R632—A new natural reference material for U-Pb and Zr determination. *Geostandards and Geoanalytical Research*, *42*, 319–338. https://doi.org/10.1111/ ggr.12213

Bell, I. A., Wilson, C. J. L., McLaren, A. C., & Etheridge, M. A. (1986). Kinks in mica: Role of dislocations and (001) cleavage. *Tectonophysics*, *127*, 49–65. https://doi.org/10.1016/0040-1951 (86)90078-8

Belousova, E. A., Walters, S., Griffin, W. L., & O'Reilly, S. Y. (2001). Trace-element signatures of apatites in granitoids from the Mt Isa Inlier, northwestern Queensland. *Australian Journal of Earth Sciences*, *48*, 603–619. https://doi.org/10.1046/j.1440-0952.2001.00879.x

Bettencourt, J. S., Leite, W. B., Ruiz, A. S., Matos, R., Payolla, B. L., & Tosdal, R. M. (2010). The Rondonian-San Ignacio Province in the SW Amazonian Craton: An overview. *Journal of South American Earth Sciences*, *29*, 28–46. https:// doi.org/10.1016/j.jsames.2009.08.006

Bispo-Santos, F., D'Agrella-Filho, M. S., Pesonen, L. J., Salminen, J. M., Reis, N. J., & Silva, J. M. (2020). The long life of SAMBA connection in Columbia: A paleomagnetic study of the 1535 Ma Mucajaí Complex, northern Amazonian Craton, Brazil. *Gondwana Research*, *80*, 285–302. https://doi.org/10. 1016/j.gr.2019.09.016

Boger, S., Raetz, M., Giles, D., Etchnart, E., & Fanning, C. (2005). U–Pb age data from the Sunsas region of Eastern Bolivia, evidence for the allochthonous origin of the Paragua Block. *Precambrian Research*, *139*, 121–146. https://doi.org/10.1016/j. precamres.2005.05.010

Bracciali, L., Parrish, R. R., Horstwood, M. S. A., Condon, D. J., & Najman, Y. (2013). UPb LA-(MC)-ICP-MS dating of rutile: New reference materials and applications to sedimentary provenance. *Chemical Geology*, *347*, 82–101. https://doi.org/10. 1016/j.chemgeo.2013.03.013

Brenan, J. M., Shaw, H. F., Phinney, D. L., & Ryerson, F. J. (1994). Rutile-aqueous fluid partitioning of Nb, Ta, Hf, Zr, U and Th: Implications for high field strength element depletions in island-arc basalts. *Earth and Planetary Science Letters*, *128*, 327–339. https://doi.org/10.1016/0012-821X(94)90154-6

Brittes, A. F. N., De Sousa, M. Z. A., Ruiz, A. S., Batata, M. E. F., Lafon, J. M., & Plens, D. P. (2013). Geology, petrology and geochronology (Pb-Pb) of the Serra da Bocaina Formation: Evidence of an Orosirian Amoguijá Magmatic Arc in the Rio Apa Terrane, south of the Amazonian Craton. *Brazilian Journal of Geology*, *43*, 48–69. https://doi.org/10.5327/Z2317-48892013000100006

Brown, M. (2010). Paired metamorphic belts revisited. *Gondwana Research*, *18*, 46–59. https://doi.org/10.1016/j.gr. 2009.11.004

Carlson, W. D., Anderson, S. D., Mosher, S., Davidow, J. S., Crawford, W. D., & Lane, E. D. (2007). High-pressure metamorphism in the Texas Grenville orogen: Mesoproterozoic subduction of the southern Laurentian continental margin. *International Geology Review*, *49*, 99–119. https://doi.org/10. 2747/0020-6814.49.2.99

Carruzzo, S., Clarke, D. B., Pelrine, K. M., & MacDonald, M. A. (2006). Texture, composition, and origin of rutile in the South Mountain Batholith, Nova Scotia. *The Canadian Mineralogist*, *44*, 715–729. https://doi.org/10.2113/gscanmin.44.3.715

Cawood, P. A., & Pisarevsky, S. A. (2017). Laurentia-Baltica-Amazonia relations during Rodinia assembly. *Precambrian Research*, *292*, 386–397. https://doi.org/10.1016/j.precamres. 2017.01.031

Černý, P., Čech, F., & Povondra, P. (1964). Review of ilmenorutile–struvertite minerals. *Neues Jahrbuch für Mineralogie Abhandlungen*, *101*, 142–172.

Černý, P., Chapman, R., Simmons, W. B., & Chackowsky, L. E. (1999). Niobian rutile from the McGuire granitic pegmatite, Park County, Colorado; solid solution, exsolution, and oxidation. *American Mineralogist*, *84*, 754–763. https://doi.org/10. 2138/am-1999-5-607

Chamberlain, K. R., & Bowring, S. A. (2000). Apatite–feldspar U–Pb thermochronometer: A reliable, mid-range (∼450°C), diffusion-controlled system. *Chemical Geology*, *172*, 173–200. https://doi.org/10.1016/S0009-2541(00)00242-4

Cherniak, D. J. (2010). Diffusion in accessory minerals: Zircon, titanite, apatite, monazite and xenotime. *Reviews in Mineralogy and Geochemistry*, *72*, 827–869. https://doi.org/10.2138/rmg. 2010.72.18

Cioffi, C. R., Neto, M. D. C. C., Möller, A., & Rocha, B. C. (2016). Paleoproterozoic continental crust generation events at 2.15 and 2.08 Ga in the basement of the southern Brasília Orogen, SE Brazil. *Precambrian Research*, *275*, 176–196. https://doi. org/10.1016/j.precamres.2016.01.007

Cioffi, C. R., Neto, M. D. C. C., Möller, A., & Rocha, B. C. (2019). Titanite petrochronology of the southern Brasília Orogen basement: Effects of retrograde net-transfer reactions on titanite trace element compositions. *Lithos*, *344–345*, 393–408. https:// doi.org/10.1016/j.lithos.2019.06.035

Cordani, U. G., Teixeira, W., Tassinari, C. C. G., Coutinho, J. M. V., & Ruiz, A. S. (2010). The Rio Apa Craton in Mato Grosso do Sul (Brazil) and northern Paraguay: Geochronological evolution, correlations and tectonic implications for Rodinia and Gondwana. *American Journal of Science*, *310*, 981–1023. https://doi.org/10.2475/09.2010.09

Dewey, J. F., Holdsworth, R. E., & Strachan, R. A. (1998). Transpression and transtension zones. In R. R. Holdsworth, R. A. Strachan, & J. E. Dewey (Eds.), *Continental transpressional and transtensional tectonic* (pp. 1–14). Geological Society, London, Special Publications.

Dos Santos, G., Ruiz, A. S., De Sousa, M. Z. A., Batata, M. E. F., Cabrera, R. F., & Lafon, J. M. (2019). Petrology, deformation and geochronology U-Pb (SHRIMP) of Coimbra Granite–Rio Apa Block in the region of Corumbá, Brazil. *Geologia USP: Serie Cientifica*, *19*, 171–192. https://doi.org/10.11606/issn.2316-9095.v19-138670

Eberlei, T., Habler, G., Wegner, W., Schuster, R., Körner, W., Thöni, M., & Abart, R. (2015). Rb/Sr isotopic and compositional retentivity of muscovite during deformation. *Lithos*, *227*, 161–178. https://doi.org/10.1016/j.lithos.2015.04.007

Evans, D. A. D. (2013). Reconstructing pre-Pangean supercontinents. *Geological Society of America Bulletin*, *125*, 1735–1751. https://doi.org/10.1130/B30950.1

Faleiros, F. M., Caltabeloti, F. P., & Pinto, L. G. R. (2014). *Programa Geologia do Brasil—PGB. Aldeia Tomázia. Folha SF.21-V-B-VI. Estado de Mato Grosso do Sul. Carta Geológica*. CPRM, 2014, 1 mapa colorido, 95 x 80 cm. Escala 1:100.000.

Faleiros, F. M., da Cruz Campanha, G. A., da Silveira Bello, R. M., & Fuzikawa, K. (2010). Quartz recrystallization regimes, c-axis texture transitions and fluid inclusion reequilibration in a prograde greenschist to amphibolite facies mylonite zone (Ribeira Shear Zone, SE Brazil). *Tectonophysics*, *485*, 193–214. https://doi.org/10.1016/j.tecto.2009.12.014

Faleiros, F. M., Pavan, M., Remédio, M. J., Rodrigues, J. B., Almeida, V. V., Caltabeloti, F. P., Pinto, L. G. R., Oliveira, A. A., Pinto de Azevedo, E. J., & Costa, V. S. (2016). Zircon U-Pb ages of rocks from the Rio Apa Cratonic Terrane (Mato Grosso do Sul, Brazil): New insights for its connection with the Amazonian Craton in pre-Gondwana times. *Gondwana Research*, *34*, 187–204. https://doi.org/10.1016/j.gr.2015.02.018

Fuhrman, M. L., & Lindsley, D. H. (1988). Ternary-feldspar modeling and thermometry. *American Mineralogist*, *73*, 201–215.

Garber, J. M., Hacker, B. R., Kylander-Clark, A. R. C., Stearns, M., & Seward, G. (2017). Controls on trace element uptake in metamorphic titanite: Implications for petrochronology. *Journal of Petrology*, *58*, 1031–1057. https://doi.org/10.1093/petrology/egx046

Giuntoli, F., Lanari, P., & Engi, M. (2018). Deeply subducted continental fragments—Part 1: Fracturing, dissolution-precipitation, and diffusion processes recorded by garnet textures of the central Sesia Zone (western Italian Alps). *Solid Earth*, *9*, 167–189. https://doi.org/10.5194/se-9-167-2018

Glodny, J., Austrheim, H., Molina, J. F., Rusin, A. I., & Seward, D. (2003). Rb/Sr record of fluid-rock interaction in eclogites: The Marun-Keu complex, Polar Urals, Russia. *Geochimica et Cosmochimica Acta*, *67*, 4353–4371. https://doi.org/10.1016/S0016-7037(03)00370-3

Glorie, S., Jepson, G., Konopelko, D., Mirkamalov, R., Meeuws, F., Gilbert, S., Gillespie, J., Collins, A. S., Xiao, W., Dewaele, S., & De Grave, J. (2019). Thermochronological and geochemical footprints of post-orogenic fluid alteration recorded in apatite: Implications for mineralisation in the Uzbek Tian Shan. *Gondwana Research*, *71*, 1–15. https://doi.org/10.1016/j.gr.2019.01.011

Gower, C. F., & Krogh, T. E. (2002). A U–Pb geochronological review of the Proterozoic history of the eastern Grenville Province. *Canadian Journal of Earth Sciences*, *39*, 795–829. https://doi.org/10.1139/e01-090

Harlov, D., Tropper, P., Seifert, W., Nijland, T., & Förster, H.-J. (2006). Formation of Al-rich titanite ($CaTiSiO_4O$–$CaAlSiO_4OH$) reaction rims on ilmenite in metamorphic rocks as a function of fH_2O and fO_2. *Lithos*, *88*, 72–84. https://doi.org/10.1016/j.lithos.2005.08.005

Hayden, L. A., Watson, E. B., & Wark, D. A. (2008). A thermobarometer for sphene (titanite). *Contributions to Mineralogy and Petrology*, *155*, 529–540. https://doi.org/10.1007/s00410-007-0256-y

Henrichs, I. A., Chew, D. M., O'Sullivan, G. J., Mark, C., McKenna, C., & Guyett, P. (2019). Trace element (Mn-Sr-Y-Th-REE) and U-Pb isotope systematics of metapelitic apatite during progressive greenschist- to amphibolite-facies Barrovian metamorphism. *Geochemistry, Geophysics, Geosystems*, *20*, 4103–4129. https://doi.org/10.1029/2019GC008359

Henrichs, I. A., O'Sullivan, G., Chew, D. M., Mark, C., Babechuk, M. G., McKenna, C., & Emo, R. (2018). The trace element and U-Pb systematics of metamorphic apatite. *Chemical Geology*, *483*, 218–238. https://doi.org/10.1016/j.chemgeo.2017.12.031

Hickman, M. H., & Glassley, W. E. (1984). The role of metamorphic fluid transport in the Rb-Sr isotopic resetting of shear zones: Evidence from Nordre Strømfjord, West Greenland. *Contributions to Mineralogy and Petrology*, *87*, 265–281. https://doi.org/10.1007/BF00373060

Hogmalm, K. J., Zack, T., Karlsson, A. K., Sjoqvist, A. S. L., & Grabe-Schonberg, D. (2017). In-situ Rb-Sr and K-Ca dating by LA-ICP-MS/MS: An evaluation of N2O and SF6 as reaction gases. *Journal of Analytical Atomic Spectrometry*, *32*, 305–313. https://doi.org/10.1039/C6JA00362A

Holder, R. M., Hacker, B. R., Seward, G. G. E., & Kylander-Clark, A. R. C. (2019). Interpreting titanite U–Pb dates and Zr thermobarometry in high-grade rocks: Empirical constraints on elemental diffusivities of Pb, Al, Fe, Zr, Nb, and Ce. *Contributions to Mineralogy and Petrology*, *174*, 1–19. https://doi.org/10.1007/s00410-019-1578-2

Holland, T. J. B., & Powell, R. (2011). An improved and extended internally consistent thermodynamic dataset for phases of petrological interest, involving a new equation of state for solids. *Journal of Metamorphic Geology*, *29*, 333–383. https://doi.org/10.1111/j.1525-1314.2010.00923.x

Honegger, K., Dietrich, V., Frank, W., Gansser, A., Thöni, M., & Trommsdorff, V. (1982). Magmatism and metamorphism in the Ladakh Himalayas (the Indus-Tsangpo suture zone). *Earth and Planetary Science Letters*, *60*, 253–292. https://doi.org/10.1016/0012-821X(82)90007-3

Hu, Z., Gao, S., Liu, Y., Hu, S., Chen, H., & Yuan, H. (2008). Signal enhancement in laser ablation ICP-MS by addition of nitrogen in the central channel gas. *Journal of Analytical Atomic Spectrometry*, *23*, 1093–1101. https://doi.org/10.1039/b804760j

Hynes, A., & Rivers, T. (2010). Protracted continental collision—Evidence from the Grenville Orogen. This article is one of a series of papers published in this Special Issue on the theme Lithoprobe—Parameters, processes, and the evolution of a continent. *Canadian Journal of Earth Sciences*, *47*, 591–620. https://doi.org/10.1139/E10-003

Inger, S., Ramsbotham, W., Cliff, R. A., & Rex, D. C. (1996). Metamorphic evolution of the Sesia-Lanzo Zone, Western Alps:

Time constraints from multi-system geochronology. *Contributions to Mineralogy and Petrology*, *126*, 152–168. https://doi.org/10.1007/s004100050241

Jepson, G., Carrapa, B., George, S. W. M., Triantafyllou, A., Egan, S. M., Constenius, K. N., Gehrels, G. E., & Ducea, M. N. (2021). Resolving mid- to upper-crustal exhumation through apatite petrochronology and thermochronology. *Chemical Geology*, *565*, 120071. https://doi.org/10.1016/j.chemgeo.2021.120071

Jiang, S.-Y., Wang, R.-C., Xu, X.-S., & Zhao, K.-D. (2005). Mobility of high field strength elements (HFSE) in magmatic-, metamorphic-, and submarine-hydrothermal systems. *Physics and Chemistry of the Earth, Parts A/B/C*, *30*, 1020–1029. https://doi.org/10.1016/j.pce.2004.11.004

Johansson, Å. (2009). Baltica, Amazonia and the SAMBA connection-1000 million years of neighbourhood during the Proterozoic? *Precambrian Research*, *175*, 221–234. https://doi.org/10.1016/j.precamres.2009.09.011

Kemp, A. I. S., Whitehouse, M. J., Hawkesworth, C. J., & Alarcon, M. K. (2005). A zircon U-Pb study of metaluminous (I-type) granites of the Lachlan Fold Belt, southeastern Australia: Implications for the high/low temperature classification and magma differentiation processes. *Contributions to Mineralogy and Petrology*, *150*, 230–249. https://doi.org/10.1007/s00410-005-0019-6

Kennedy, A. K., Kamo, S. L., Nasdala, L., & Timms, N. E. (2010). Grenville skarn titanite: Potential reference material for Sims U-Th–Pb analysis. *The Canadian Mineralogist*, *48*, 1423–1443. https://doi.org/10.3749/canmin.48.5.1423

Kirkland, C. L., Hollis, J., Danišík, M., Petersen, J., Evans, N. J., & McDonald, B. J. (2017). Apatite and titanite from the Karrat Group, Greenland; implications for charting the thermal evolution of crust from the U-Pb geochronology of common Pb bearing phases. *Precambrian Research*, *300*, 107–120. https://doi.org/10.1016/j.precamres.2017.07.033

Kirkland, C. L., Yakymchuk, C., Gardiner, N. J., Szilas, K., Hollis, J., Olierook, H., & Steenfelt, A. (2020). Titanite petrochronology linked to phase equilibrium modelling constrains tectono-thermal events in the Akia Terrane, West Greenland. *Chemical Geology*, *536*, 119467. https://doi.org/10.1016/j.chemgeo.2020.119467

Lacerda Filho, J. V., Fuck, R. A., Ruiz, A. S., Dantas, E. L., Rodrigues, J. B., & Scandolara, J. E. (2020). Rio Apa Block: A juvenile crustal fragment in the southwest Amazonian Craton and its implications for Columbia supercontinent reconstitution. *Journal of Geology*, *128*, 415–444. https://doi.org/10.1086/710999

Lacerda Filho, J. V., Fuck, R. A., Ruiz, A. S., Dantas, E. L., Scandolara, J. E., Rodrigues, J. B., & Nascimento, N. D. C. (2016). Palaeoproterozoic tectonic evolution of the Alto Tererê Group, southernmost Amazonian Craton, based on field mapping, zircon dating and rock geochemistry. *Journal of South American Earth Sciences*, *65*, 122–141. https://doi.org/10.1016/j.jsames.2015.11.001

Lanari, P., & Duesterhoeft, E. (2019). Modeling metamorphic rocks using equilibrium thermodynamics and internally consistent databases: Past achievements, problems and perspectives. *Journal of Petrology*, *60*, 19–56. https://doi.org/10.1093/petrology/egy105

Lanari, P., & Engi, M. (2017). Local bulk composition effects on metamorphic mineral assemblages. *Reviews in Mineralogy and Geochemistry*, *83*, 55–102. https://doi.org/10.2138/rmg.2017.83.3

Lanari, P., Giuntoli, F., Loury, C., Burn, M., & Engi, M. (2017). An inverse modeling approach to obtain P–T conditions of metamorphic stages involving garnet growth and resorption. *European Journal of Mineralogy*, *29*, 181–199. https://doi.org/10.1127/ejm/2017/0029-2597

Lanari, P., Riel, N., Guillot, S., Vidal, O., Schwartz, S., Pêcher, A., & Hattori, K. H. (2013). Deciphering high-pressure metamorphism in collisional context using microprobe mapping methods: Application to the Stak eclogitic massif (northwest Himalaya). *Geology*, *41*, 111–114. https://doi.org/10.1130/G33523.1

Lanari, P., Vho, A., Bovay, T., Airaghi, L., & Centrella, S. (2019). Quantitative compositional mapping of mineral phases by electron probe micro-analyser. *Geological Society, London, Special Publications*, *478*, 39–63. https://doi.org/10.1144/SP478.4

Lanari, P., Vidal, O., De Andrade, V., Dubacq, B., Lewin, E., Grosch, E. G., & Schwartz, S. (2014). XMapTools: A MATLAB©-based program for electron microprobe X-ray image processing and geothermobarometry. *Computational Geosciences*, *62*, 227–240. https://doi.org/10.1016/j.cageo.2013.08.010

Lane, K. (2011). *Metamorphic and geochronological constraints on the evolution of the Kalinjala Shear Zone*. The University of Adelaide.

Launeau, P., & Robin, P. Y. F. (2005). Determination of fabric and strain ellipsoids from measured sectional ellipses—Implementation and applications. *Journal of Structural Geology*, *27*, 2223–2233. https://doi.org/10.1016/j.jsg.2005.08.003

Li, Y., & Vermeesch, P. (2021). Inverse isochron regression for Re-Os, K-Ca and other chronometers. *Geochronology Discussions*, *3*, 415–420. https://doi.org/10.5194/gchron-2021-7

Manzano, J. C., Godoy, A. M., Araujo, L. M. B., & Godoy, L. P. (2012). Suite plutônica Alumiador, Grupo Amoguijá, Maciço Rio Apa-MS. *Geociências*, *31*, 351–370.

McDonough, W. F., & Sun, S. S. (1995). The composition of the Earth. *Chemical Geology*, *2541*, 223–253. https://doi.org/10.1016/0009-2541(94)00140-4

Michailidis, K. M. (1997). An EPMA and SEM study of niobian–tungstenian rutile from the Fanos aplitic granite, central Macedonia, northern Greece. *Neues Jahrbuch für Mineralogie Monatshefte*, *12*, 549–563.

Mosher, S., Levine, J. S. F., & Carlson, W. D. (2008). Mesoproterozoic plate tectonics: A collisional model for the Grenville-aged orogenic belt in the Llano uplift, central Texas. *Geology*, *36*, 55–58. https://doi.org/10.1130/G24049A.1

Nebel, O., Morel, M. L. A., & Vroon, P. Z. (2009). Isotope dilution determinations of Lu, Hf, Zr, Ta and W, and Hf isotope compositions of NIST SRM 610 and 612 glass wafers. *Geostandards and Geoanalytical Research*, *33*, 487–499. https://doi.org/10.1111/j.1751-908X.2009.00032.x

Nedel, I. M. (2020). *Evolução crustal da Faixa Sunsás, SW do Cráton Amazônico*. University of Brasilia.

Nedel, I. M., Fuck, R. A., Ruiz, A. S., Matos-Salinas, G. R., & da CD Ferreira, A. (2021). Timing of Proterozoic magmatism in the Sunsás belt, Bolivian Precambrian Shield, SW Amazonian

Craton. *Geoscience Frontiers*, *12*(6), 101247. https://doi.org/10.1016/j.gsf.2021.101247

Norris, A., & Danyushevsky, L. (2018). *Towards estimating the complete uncertainty budget of quantified results measured be LA-ICP-MS*. Goldschmidt Abstracts.

Odlum, M. L., & Stockli, D. F. (2020). Geochronologic constraints on deformation and metasomatism along an exhumed mylonitic shear zone using apatite U-Pb, geochemistry, and microtextural analysis. *Earth and Planetary Science Letters*, *538*, 116177. https://doi.org/10.1016/j.epsl.2020.116177

Olierook, H. K. H., Rankenburg, K., Ulrich, S., Kirkland, C. L., Evans, N. J., Brown, S., McInnes, B. I. A., Prent, A., Gillespie, J., McDonald, B., & Darragh, M. (2020). Resolving multiple geological events using in situ Rb–Sr geochronology: Implications for metallogenesis at Tropicana, Western Australia. *Geochronology*, *2*, 283–303. https://doi.org/10.5194/gchron-2-283-2020

O'Neill, H. S. C. (2016). The smoothness and shapes of chondrite-normalized rare earth element patterns in basalts. *Journal of Petrology*, *57*, 1463–1508. https://doi.org/10.1093/petrology/egw047

Oriolo, S., Wemmer, K., Oyhantçabal, P., Fossen, H., Schulz, B., & Siegesmund, S. (2018). Geochronology of shear zones—A review. *Earth-Science Reviews*, *185*, 665–683. https://doi.org/10.1016/j.earscirev.2018.07.007

O'Sullivan, G., Chew, D., Kenny, G., Henrichs, I., & Mulligan, D. (2020). The trace element composition of apatite and its application to detrital provenance studies. *Earth-Science Reviews*, *201*, 103044. https://doi.org/10.1016/j.earscirev.2019.103044

O'Sullivan, G. J., Thakurdin, Y., Bolhar, R., Horváth, P., Hoare, B. C., & Collerson, K. D. (2021). The Great Falls Tectonic Zone after the assembly of Laurentia: Evidence for long-term tectonic stability from xenolith apatite. *Lithos*, *384–385*, 105977. https://doi.org/10.1016/j.lithos.2021.105977

Papapavlou, K., Darling, J. R., Storey, C. D., Lightfoot, P. C., Moser, D. E., & Lasalle, S. (2017). Dating shear zones with plastically deformed titanite: New insights into the orogenic evolution of the Sudbury impact structure (Ontario, Canada). *Precambrian Research*, *291*, 220–235. https://doi.org/10.1016/j.precamres.2017.01.007

Passchier, C. W., & Trouw, R. A. J. (2005). *Microtectonics* (2nd ed.). Springer.

Paton, C., Hellstrom, J., Paul, B., Woodhead, J., & Hergt, J. (2011). Iolite: Freeware for the visualisation and processing of mass spectrometric data. *Journal of Analytical Atomic Spectrometry*, *26*, 2508–2518. https://doi.org/10.1039/c1ja10172b

Paton, C., Woodhead, J. D., Hellstrom, J. C., Hergt, J. M., Greig, A., & Maas, R. (2010). Improved laser ablation U-Pb zircon geochronology through robust downhole fractionation correction. *Geochemistry, Geophysics, Geosystems*, *11*, n/a–n/a. https://doi.org/10.1029/2009GC002618

Payne, J. L., Hand, M., Barovich, K. M., & Wade, B. P. (2008). Temporal constraints on the timing of high-grade metamorphism in the northern Gawler Craton: Implications for assembly of the Australian Proterozoic. *Australian Journal of Earth Sciences*, *55*, 623–640. https://doi.org/10.1080/08120090801982595

Plens, D. P. (2018). *Petrogenese e análise estrutural da Suíte Caracol: implicações para a evolução geodinâmica do Bloco Rio Apa - Sul do Cráton Amazônico*. University of Brasilia.

Plens, D. P., Ruiz, A. S., de Sousa, M. Z. A., Batata, M. E. F., Lafon, J. M., & Brittes, A. F. N. (2013). Cerro Porã Batholith: Post-orogenic A-type granite from the Amoguijá Magmatic Arc-Rio Apa Terrane-South of the Amazonian Craton. *Brazilian Journal of Geology*, *43*, 515–534. https://doi.org/10.5327/Z2317-48892013000300008

Pollington, A. D., & Baxter, E. F. (2010). High resolution Sm–Nd garnet geochronology reveals the uneven pace of tectonometamorphic processes. *Earth and Planetary Science Letters*, *293*, 63–71. https://doi.org/10.1016/j.epsl.2010.02.019

Porter, J. K., McNaughton, N. J., Evans, N. J., & McDonald, B. J. (2020). Rutile as a pathfinder for metals exploration. *Ore Geology Reviews*, *120*, 103406. https://doi.org/10.1016/j.oregeorev.2020.103406

Putnis, A. (1978). The mechanism of exsolution of hematite from iron-bearing rutile. *Physics and Chemistry of Minerals*, *3*, 183–197. https://doi.org/10.1007/BF00308121

Putnis, A., & Wilson, M. M. (1978). A study of iron-bearing rutiles in the paragenesis. *Mineralogical Magazine*, *42*, 255–263. https://doi.org/10.1180/minmag.1978.042.322.14

Redes, L. A., Hauser, N., Ruiz, A. S., Matos, R. S., Reimold, W. U., Dantas, E. L., Schmitt, R.-T., Lima, B. A. F., Zacchi, E. N. P., Silva Chaves, J. G., Baumotte Osorio, L. F., & Pimentel, M. M. (2020). U–Pb and Hf isotopes in granitoids from the Eastern Bolivian basement: Insights into the Paleoproterozoic evolution of the western part of South America. *Journal of South American Earth Sciences*, *104*, 102806. https://doi.org/10.1016/j.jsames.2020.102806

Redes, L. A., Sousa, M. Z. A. D., Ruiz, A. S., & Lafon, J.-M. (2015). Petrogenesis and U-Pb and Sm-Nd geochronology of the Taquaral granite: Record of an orosirian continental magmatic arc in the region of Corumba-MS. *Brazilian Journal of Geology*, *45*, 431–451. https://doi.org/10.1590/2317-488920150030231

Rezvukhina, O. V., Skublov, S. G., Rezvukhin, D. I., & Korsakov, A. V. (2021). Rutile in diamondiferous metamorphic rocks: New insights from trace-element composition, mineral/fluid inclusions, and U-Pb ID-TIMS dating. *Lithos*, *394–395*, 106172. https://doi.org/10.1016/j.lithos.2021.106172

Ribeiro, B. V., Cawood, P. A., Faleiros, F. M., Mulder, J. A., Martin, E., Finch, M. A., Raveggi, M., Teixeira, W., Cordani, U. G., & Pavan, M. (2020). A long-lived active margin revealed by zircon U–Pb–Hf data from the Rio Apa Terrane (Brazil): New insights into the Paleoproterozoic evolution of the Amazonian Craton. *Precambrian Research*, *350*, 105919. https://doi.org/10.1016/j.precamres.2020.105919

Ribeiro, B. V., Faleiros, F. M., Campanha, G. A. C., Lagoeiro, L., Weinberg, R. F., & Hunter, N. J. R. (2019). Kinematics, deformational conditions and tectonic setting of the Taxaquara Shear Zone, a major transpressional zone of the Ribeira Belt (SE Brazil). *Tectonophysics*, *751*, 83–108. https://doi.org/10.1016/j.tecto.2018.12.025

Ribeiro, B. V., Lagoeiro, L., Faleiros, F. M., Hunter, N. J. R., Queiroga, G., Raveggi, M., Cawood, P. A., Finch, M., & Campanha, G. A. C. (2020). Strain localization and fluid-assisted deformation in apatite and its influence on trace elements and U–Pb systematics. *Earth and Planetary Science Letters*, *545*, 116421. https://doi.org/10.1016/j.epsl.2020.116421

Ribeiro, B. V., Mulder, J. A., Faleiros, F. M., Kirkland, C. L., Cawood, P. A., O'Sullivan, G., Campanha, G. A. C.,

Finch, M. A., Weinberg, R. F., & Nebel, O. (2020). Using apatite to resolve the age and protoliths of mid-crustal shear zones: A case study from the Taxaquara Shear Zone, SE Brazil. *Lithos*, *378–379*, 105817. https://doi.org/10.1016/j.lithos.2020.105817

Rivers, T., & Corrigan, D. (2000). Convergent margin on southeastern Laurentia during the Mesoproterozoic: Tectonic implications. *Canadian Journal of Earth Sciences*, *37*, 359–383. https://doi.org/10.1139/e99-067

Rizzotto, G. J., Santos, J. O. S., Hartmann, L. A., Tohver, E., Pimentel, M. M., & McNaughton, N. J. (2013). The Mesoproterozoic Guaporé suture in the SW Amazonian Craton: Geotectonic implications based on field geology, zircon geochronology and Nd–Sr isotope geochemistry. *Journal of South American Earth Sciences*, *48*, 271–295. https://doi.org/10.1016/j.jsames.2013.10.001

Rocha, B. C., Moraes, R., Möller, A., Cioffi, C. R., & Jercinovic, M. J. (2017). Timing of anatexis and melt crystallization in the Socorro–Guaxupé Nappe, SE Brazil: Insights from trace element composition of zircon, monazite and garnet coupled to U–Pb geochronology. *Lithos*, *277*, 337–355. https://doi.org/10.1016/j.lithos.2016.05.020

Rocha, M. P., Assumpção, M., Affonso, G. M. P. C., Azevedo, P. A., & Bianchi, M. (2019). Teleseismic P wave tomography beneath the Pantanal, Paraná, and Chaco-Paraná basins, SE South America: Delimiting lithospheric blocks of the SW Gondwana assemblage. *Journal of Geophysical Research - Solid Earth*, *124*, 7120–7137. https://doi.org/10.1029/2018JB016807

Romer, R., & Smeds, S.-A. (1996). U-Pb columbite ages of pegmatites from Sveconorwegian terranes in southwestern Sweden. *Precambrian Research*, *76*, 15–30. https://doi.org/10.1016/0301-9268(95)00023-2

Sadowski, G. R., & Bettencourt, J. S. (1996). Mesoproterozoic tectonic correlations between eastern Laurentia and the western border of the Amazon Craton. *Precambrian Research*, *76*, 213–227. https://doi.org/10.1016/0301-9268(95)00026-7

Santamaría-López, Á., Lanari, P., & Sanz de Galdeano, C. (2019). Deciphering the tectono-metamorphic evolution of the Nevado-Filábride complex (Betic Cordillera, Spain)—A petrochronological study. *Tectonophysics*, *767*, 128–158. https://doi.org/10.1016/j.tecto.2019.06.028

Schoene, B., & Bowring, S. A. (2006). U-Pb systematics of the McClure Mountain syenite: Thermochronological constraints on the age of the ^{40}Ar/^{39}Ar standard MMhb. *Contributions to Mineralogy and Petrology*, *151*, 615–630. https://doi.org/10.1007/s00410-006-0077-4

Scodina, M., Cruciani, G., Franceschelli, M., & Massonne, H.-J. (2019). Anticlockwise P-T evolution of amphibolites from NE Sardinia, Italy: Geodynamic implications for the tectonic evolution of the Variscan Corsica-Sardinia block. *Lithos*, *324–325*, 763–775. https://doi.org/10.1016/j.lithos.2018.12.003

Scott, K. M., & French, D. H. (2005). Rutile geochemistry as a guide to mineralization at the Escondida Cu deposit, Chile. *15th Annual V M Goldschmidt Conference*, *69*, A60.

Scott, K. M., Radford, N. W., Hough, R. M., & Reddy, S. M. (2011). Rutile compositions in the Kalgoorlie Goldfields and their implications for exploration. *Australian Journal of Earth Sciences*, *58*, 803–812. https://doi.org/10.1080/08120099.2011.600334

Sha, L.-K., & Chappell, B. W. (1999). Apatite chemical composition, determined by EMP and laser-ablation ICP-MS, as a probe into granite petrogenesis. *Geochimica et Cosmochimica Acta*, *63*, 3861–3881. https://doi.org/10.1016/S0016-7037(99)00210-0

Simpson, A., Gilbert, S., Tamblyn, R., Hand, M., Spandler, C., Gillespie, J., Nixon, A., & Glorie, S. (2021). In-situ Lu Hf geochronology of garnet, apatite and xenotime by LA ICP MS/MS. *Chemical Geology*, *577*, 120299. https://doi.org/10.1016/j.chemgeo.2021.120299

Söderlund, U., Patchett, P. J., Vervoort, J. D., & Isachsen, C. E. (2004). The 176Lu decay constant determined by Lu–Hf and U–Pb isotope systematics of Precambrian mafic intrusions. *Earth and Planetary Science Letters*, *219*, 311–324. https://doi.org/10.1016/S0012-821X(04)00012-3

Souza, C., Sousa, M. Z., Ruiz, A., Batata, M. E., Brittes, A. F., & Lafon, J.-M. (2017). Formação Serra da Bocaina: Contribuição do vulcanismo paleoproterozoico do arco magmático Amoguijá no bloco Rio Apa, Sul do Cráton Amazônico. *Geochimica Brasiliensis*, *30*, 136–157. https://doi.org/10.21715/gb2358-2812.2016302136

Spencer, C. J., Hawkesworth, C., Cawood, P. A., & Dhuime, B. (2013). Not all supercontinents are created equal: Gondwana-Rodinia case study. *Geology*, *41*, 795–798. https://doi.org/10.1130/G34520.1

Stacey, J. S., & Kramers, J. D. (1975). Approximation of terrestrial lead isotope evolution by a two-stage model. *Earth and Planetary Science Letters*, *26*, 207–221. https://doi.org/10.1016/0012-821X(75)90088-6

Stipp, M., Stünitz, H., Heilbronner, R., & Schmid, S. M. (2002a). The eastern Tonale fault zone: A "natural laboratory" for crystal plastic deformation of quartz over a temperature range from 250 to 700 °C. *Journal of Structural Geology*, *24*, 1861–1884. https://doi.org/10.1016/S0191-8141(02)00035-4

Stipp, M., Stünitz, H., Heilbronner, R., & Schmid, S. M. (2002b). Dynamic recrystallization of quartz: Correlation between natural and experimental conditions. *Geological Society, London, Special Publications*, *200*, 171–190. https://doi.org/10.1144/GSL.SP.2001.200.01.11

Teixeira, W., Cordani, U. G., Faleiros, F. M., Sato, K., Maurer, V. C., Ruiz, A. S., & Azevedo, E. J. P. (2020). The Rio Apa Terrane reviewed: U–Pb zircon geochronology and provenance studies provide paleotectonic links with a growing Proterozoic Amazonia. *Earth-Science Reviews*, *202*, 103089. https://doi.org/10.1016/j.earscirev.2020.103089

Thomson, S. N., Gehrels, G. E., Ruiz, J., & Buchwaldt, R. (2012). Routine low-damage apatite U-Pb dating using laser ablation–multicollector–ICPMS. *Geochemistry, Geophysics, Geosystems*, *13*(2). https://doi.org/10.1029/2011GC003928

Tollo, R. P., & Haggerty, S. R. (1987). Nb-Cr-rutile in the Orapa kimberlite, Botswana. *The Canadian Mineralogist*, *25*, 251–264.

Tomkins, H. S., Powell, R., & Ellis, D. J. (2007). The pressure dependence of the zirconium-in-rutile thermometer. *Journal of Metamorphic Geology*, *25*, 703–713. https://doi.org/10.1111/j.1525-1314.2007.00724.x

Van Daele, J., Dewaele, S., Melcher, F., Onuk, P., Spikings, R., Glorie, S., Jepson, G., & Muchez, P. (2020). Geochronology of

metamorphism, deformation and fluid circulation: A comparison between and Ar-Ar phyllosilicate and U-Pb apatite systematics in the Karagwe-Ankole Belt (Central Africa). *Gondwana Research*, *83*, 279–297. https://doi.org/10.1016/j.gr.2020.02.008

Vermeesch, P. (2013). Multi-sample comparison of detrital age distributions. *Chemical Geology*, *341*, 140–146. https://doi.org/10.1016/j.chemgeo.2013.01.010

Vermeesch, P. (2018). IsoplotR: A free and open toolbox for geochronology. *Geoscience Frontiers*, *9*, 1479–1493. https://doi.org/10.1016/j.gsf.2018.04.001

Vermeesch, P., Resentini, A., & Garzanti, E. (2016). An R package for statistical provenance analysis. *Sedimentary Geology*, *336*, 14–25. https://doi.org/10.1016/j.sedgeo.2016.01.009

Vervoort, J. D., Plank, T., & Prytulak, J. (2011). The Hf-Nd isotopic composition of marine sediments. *Geochimica et Cosmochimica Acta*, *75*, 5903–5926. https://doi.org/10.1016/j.gca.2011.07.046

Vho, A., Rubatto, D., Lanari, P., Giuntoli, F., Regis, D., & Hermann, J. (2020). Crustal reworking and hydration: Insights from element zoning and oxygen isotopes of garnet in high-pressure rocks (Sesia Zone, Western Alps). *Contributions to Mineralogy and Petrology*, *175*, 1–28. https://doi.org/10.1007/s00410-020-01745-6

Villa, I. M., De Bièvre, P., Holden, N. E., & Renne, P. R. (2015). IUPAC-IUGS recommendation on the half life of 87Rb. *Geochimica et Cosmochimica Acta*, *164*, 382–385. https://doi.org/10.1016/j.gca.2015.05.025

Villa, I. M., & Williams, M. L. (2013). *Geochronology of metasomatic events*. Lecture Notes in Earth System Sciences. Springer. https://doi.org/10.1007/978-3-642-28394-9

Volante, S., Pourteau, A., Collins, W. J., Blereau, E., Li, Z. X., Smit, M., Evans, N. J., Nordsvan, A. R., Spencer, C. J., McDonald, B. J., Li, J., & Günter, C. (2020). Multiple P–T–d–t paths reveal the evolution of the final Nuna assembly in northeast Australia. *Journal of Metamorphic Geology*, *38*, 593–627. https://doi.org/10.1111/jmg.12532

Wan, B., Windley, B. F., Xiao, W., Feng, J., & Zhang, J. (2015). Paleoproterozoic high-pressure metamorphism in the northern North China Craton and implications for the Nuna supercontinent. *Nature Communications*, *6*, 1, 8344–10. https://doi.org/10.1038/ncomms9344

White, R. W., Powell, R., Holland, T. J. B., & Worley, B. (2000). The effect of TiO_2 and Fe_2O_3 on metapelitic assemblages at greenschist and amphibolite facies conditions: Mineral equilibria calculations in the system $K_2O–FeO–MgO–Al_2O_3–SiO_2–H_2O–TiO_2–Fe_2O_3$. *Journal of Metamorphic Geology*, *18*, 497–511. https://doi.org/10.1046/j.1525-1314.2000.00269.x

White, R. W., Powell, R., & Johnson, T. E. (2014). The effect of Mn on mineral stability in metapelites revisited: New *a–x* relations for manganese-bearing minerals. *Journal of Metamorphic Geology*, *32*, 809–828. https://doi.org/10.1111/jmg.12095

Whitney, D. L., & Evans, B. W. (2010). Abbreviations for names of rock-forming minerals. *American Mineralogist*, *95*, 185–187. https://doi.org/10.2138/am.2010.3371

Wilson, C. J. L., & Bell, I. A. (1979). Deformation of biotite and muscovite: Optical microstructure. *Tectonophysics*, *58*, 179–200. https://doi.org/10.1016/0040-1951(79)90328-7

Xu, Z.-Q., Dilek, Y., Yang, J.-S., Liang, F.-H., Liu, F., Ba, D.-Z., Cai, Z.-H., Li, G.-W., Dong, H.-W., & Ji, S.-C. (2015). Crustal structure of the Indus–Tsangpo suture zone and its ophiolites in southern Tibet. *Gondwana Research*, *27*, 507–524. https://doi.org/10.1016/j.gr.2014.08.001

Zack, T., & Hogmalm, K. J. (2016). Laser ablation Rb/Sr dating by online chemical separation of Rb and Sr in an oxygen-filled reaction cell. *Chemical Geology*, *437*, 120–133. https://doi.org/10.1016/j.chemgeo.2016.05.027

Zack, T., Moraes, R., & Kronz, A. (2004). Temperature dependence of Zr in rutile: Empirical calibration of a rutile thermometer. *Contributions to Mineralogy and Petrology*, *148*, 471–488. https://doi.org/10.1007/s00410-004-0617-8

Zoleikhaei, Y., Mulder, J. A., & Cawood, P. A. (2021). Integrated detrital rutile and zircon provenance reveals multiple sources for Cambrian sandstones in North Gondwana. *Earth-Science Reviews*, *213*, 103462. https://doi.org/10.1016/j.earscirev.2020.103462

SUPPORTING INFORMATION

Additional supporting information may be found in the online version of the article at the publisher's website.

Table S1: Chemical mineral composition from electron probe microanalyses
Table S2: Apatite U–Pb–REE data
Table S3: Titanite U–Pb–REE data
Table S4: Rutile U–Pb–REE data
Table S5: U–Pb–REE standard results
Table S6: In-situ Rb-Sr data from standards and unknowns
Table S7: In-situ Lu-Hf data from garnet standards and unknowns